Andreas Wagner, BSc

Computing Coronal Magnetic Field Lines using EUHFORIA - Parameter testing, model development and comparison to observations

MASTER'S THESIS

to achieve the university degree of

Master of Science

Master's degree programme:

Physics

submitted to

Graz University of Technology

Supervisor

Assoz. Prof. Mag. Dr.rer.nat. Manuela Temmer

University of Graz, Institute of Physics

Eleanna Asvestari, PhD.

University of Helsinki, Department of Physics

Graz, May 2021

AFFIDAVIT

I declare that I have authored this thesis independently, that I have not used other than the declared sources/resources, and that I have explicitly indicated all material which has been quoted either literally or by content from the sources used. The text document uploaded to TUGRAZonline is identical to the present master's thesis.

Date, Signature

Abstract

While the Sun provides us with the necessary conditions for our life on Earth, there are also dangers originating from our host star. Various effects of the solar activity that can cause harm for us and our technologies are summarized under the term "space weather". To predict such space weather events a variety of simulation codes exist. As their basis they need a magnetic field model for the solar atmosphere (the solar corona). Testing and assessing the accuracy of such models is crucial for the development of future space weather forecasting codes. In this thesis we investigate the coronal magnetic field model of EUHFORIA (EUropean Heliospheric FORcasting Information Asset), which consists of a PFSS (Potential Field Source Surface) model, coupled to an SCS (Schatten Current Sheet) model. This constellation possesses two free parameters: the source surface height $R_{\rm ss}$ and the Schatten current sheet height $R_{\rm scs}$. We aimed at varying these parameters, resulting in 67 different configurations, to find an ideal parameter set for the model. To achieve this we developed a novel assessment scheme that makes use of white-light data, as well as EUV (extreme ultraviolet) data. Following our analysis, the best performing parameter set is $[R_{\rm scs} = 2.0{\rm R}_\odot, R_{\rm ss} = 2.4{\rm R}_\odot]$, which is close to current default values (see e.g. Pomoell and Poedts, 2018).

Keywords: Magnetic fields, Solar corona, Solar-terrestrial relations

Zusammenfassung

Obwohl die Sonne die nötigen Bedingungen für das Leben auf der Erde liefert gehen auch Gefahren von unserem Wirtsstern aus. Verschiedene Effekte der Sonnenaktivität welche uns und unsere Technologien bedrohen werden unter der Bezeichnung "Weltraumwetter" zusammengefasst. Um Vorhersagen zu derartigen Weltraumwetterevents zu treffen gibt es einige Simulationscodes. Am Fundament benötigen diese ein Modell des Magnetfelds der Sonnenatmosphäre (Sonnenkorona). Das Testen und Beurteilen derer Genauigkeit ist essenziell für die Entwicklung zukünftiger Weltraumwetter-Simulationscodes. In dieser Arbeit haben wir das koronale Magnetfeldmodell von EUHFORIA (EUropean Heliospheric FORcasting Information Asset) untersucht, welches aus einem PFSS (Potential Field Source Surface) Modell und einem SCS (Schatten Current Sheet) Modell besteht. Diese Konstellation besitzt zwei freie Parameter: die "source surface height" R_{ss} und die "Schatten current sheet height" R_{scs}. Wir zielten auf das Variieren der Parameter ab, was zu 67 verschiedenen Konfigurationen führte, um ein ideales Parameterset zu finden. Um dies zu erreichen entwickelten wir ein Beurteilungsschema welches auf Weißlichtdaten und EUV-Daten (EUV = Extremes Ultraviolett) beruht. Unserer Analyse zufolge ist das beste Parameterset $[R_{\mathrm{scs}} = 2.0\mathrm{R}_{\odot}, R_{\mathrm{ss}} = 2.4\mathrm{R}_{\odot}]$, was nahe der aktuellen Defaultwerte liegt (siehe z.B. Pomoell and Poedts, 2018).

Acknowledgements

Special thanks to my supervisor Manuela Temmer for the immense support not only during my work on the thesis but also throughout my Master's studies. I learned so much not only about solar physics, but also about working in the science community. I can confidently say that it will be a difficult task for anyone to match this high level of quality as a supervisor. Moreover, I want to thank my co-supervisor Eleanna Asvestari for the productive discussions and for helping me out getting started with my work and with the setup of the EUHFORIA code. I appreciate a lot that you found time this often, despite the distance and your busy schedules. I thank my parents for the support and being part in developing my scientific interest from an early age on. Also, I want to thank former and current office colleagues, especially Stephan Heinemann, Stefan Hofmeister and Manu Gupta. Special thanks to my friend and former room mate Joshua Hoffer for countless hours of physical discussions and for pushing through with our studies together. Your great ambitions also sparked my eagerness to work harder every day to pursue my goals in science.

This thesis made use of the infrastructure, resources and observational facilities of the Department for Geophysics, Astrophysics and Meteorology (IGAM) at the Institute of Physics of the University of Graz. I thank Roland Maderbacher and Klaus Huber for maintaining the IT-infrastructure, software installations, the server farm and providing technical support, whenever needed. The team of UniIT is thanked for maintaining and supporting the use of the high performance cluster (HPC), used for computations presented in this thesis.

I thank the people behind the space missions, whose data we were using in this thesis, namely the STEREO, SOHO, SDO and PROBA-2 missions. Furthermore, I thank the people behind the ground-based data we were using, i.e., GONG and MWO, as well as Miloslav Druckmüller's high-resolution eclipse images.

Contents

1 Introduction

1.1 The Sun

The Sun is essential for life on Earth, providing ideal conditions for our existence. It has a radius of roughly $R = 7 \cdot 10^8$ m and a mass of about $M = 2 \cdot 10^{30}$ kg. Probably the most essential property for the habitability of our planet though is the effective temperature at $T_{\text{eff}} = 5772$ K (defined by the International Astronomical Union in 2015). This temperature is strongly tied to the solar luminosity L, via the following relation:

$$L = 4\pi R^2 \sigma T_{\text{eff}}^4$$

Here, $\sigma = 5.67 \cdot 10^{-8} \frac{\text{W}}{\text{m}^2\text{K}^4}$ represents the Stefan-Boltzmann constant. With these quantities one can generate the so-called Hertzsprung-Russell diagram, which shows a star's temperature over its luminosity. In Figure 1.1 one can see that, while the Sun's properties sound pretty impressive, they are quite ordinary on a stellar scale. Thus, the Sun is located on the main sequence together with over 90% of other stars (Hanslmeier, 2014).

1.1.1 The Solar Interior

The energy that is needed to produce the above given luminosity originates from its own interior by the means of nuclear fusion. In detail, it is mostly hydrogen that is fused to helium in a chain of reactions called the pp-chain (see e.g., Aschwanden, 2019):

$$p + p \rightarrow {}^2He + e^+ + \nu_e$$

$${}^2He + p \rightarrow {}^3He + \gamma$$

$${}^3He + {}^3He \rightarrow {}^4He + p + p$$

It should be noted that this is not necessarily the prime fusion mechanisms for other stars, because, as it is usually the case with chemical reactions, they are highly dependent on the surrounding conditions such as pressure and temperature. For

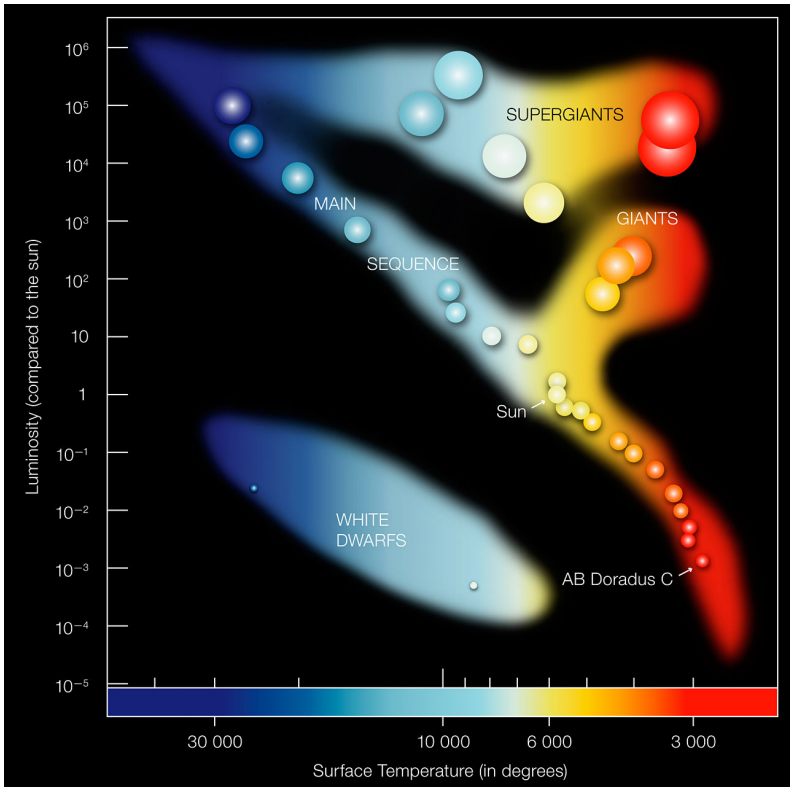

Fig. 1.1.: Hertzsprung-Russell diagram and the Sun's position. The image is taken from ESO (European Southern Observatory).

more massive stars for example the CNO-cycle is the dominant one. A common result though for all stars is that for each fusion reaction a certain amount of energy is set free - in the case of the pp-chain it is $E = 26.73$ MeV (see e.g., Aschwanden, 2019). These processes are happening directly in the solar core and thus measuring the resulting neutrino fluxes gives us information about this region of the solar interior. Actually the measurement of the solar neutrino flux has been a long time problem in solar and theoretical physics as the predictions from solar models did not correspond to the measurements. This is known under the term "solar neutrino problem". While the actual problem has been that the theory of electroweak physics at that time had no inclusion of neutrino oscillations, attempts to explain the discrepancies have been made in the form of "revised" solar models (Bahcall et al., 2001). Because as can be seen above, all neutrinos originating from the pp-chain should be electron neutrinos. The problem was solved in 2001 by the Sudbury Neutrino Observatory (SNO) that first measured not only the originally expected electron-neutrino ν_e but also the other two flavours, being the muon neutrino ν_μ and the tauon neutrino ν_τ (Aschwanden, 2019). Therefore they captured the total solar neutrino flux.

The shells that envelop the solar core are named by their primary energy transport mechanism: the radiation zone and the convection zone. The radiation zone is the inner of the two layers. For cool stars (like the Sun) the outer parts are convectively

unstable. Convection sets in when the radiative gradient surpasses the adiabatic gradient, which is called the Schwarzschild-criterion (see e.g., Hanslmeier, 2014):

$$\left|\frac{dT}{dR}\right|_{rad} > \left|\frac{dT}{dR}\right|_{ad}$$

R is the radius and T is the temperature. With this the transition of radiation to convection zone can be explained. Convection is efficient until reaching the photospheric level, where the density drops.

1.1.2 The Photosphere and Chromosphere

The photosphere is the layer which defines the Sun's surface. As the Sun is not a solid body, another definition other than a solid edge has to be made to define a "surface". As typical with stars, it is defined by the layer which emits most of its light. Compared to the full extension of our host star, the thickness of the photosphere is rather thin with about 400 km (see e.g., Hanslmeier, 2014). It is also the layer where a magnetic phenomenon called sunspots can be observed. These are dark structures of high magnetic field strengths. The lowered intensity in those regions originates from the stronger magnetic field: By applying the ideal gas equation, where the pressure p is linearly proportional to the temperature T, and the fact that additionally to the gas pressure there is also a heightened magnetic pressure one can see that T has to decrease in those regions. Lower temperatures correspond to lowered radiation by the Stefan-Boltzmann law:

$$E = \sigma \cdot T^4$$

Here, σ is again the Stefan-Boltzmann constant, E is the radiant emittance, which is the radiated energy per time per area over all wavelengths. Those regions are of great importance, because they are a indicator of the current solar activity (see Section 1.3). Instead of counting individual sunspots, Johann Rudolf Wolf invented a counting scheme, called the relative sunspot number, which is defined as follows:

$$R = k(10g + n)$$

where k accounts for the observer's bias, g is the number of sunspot groups and n the number of isolated spots (see e.g., Hathaway, 2015). The photosphere is also host for the so-called granulation, which is formed by hydrodynamic convection cells

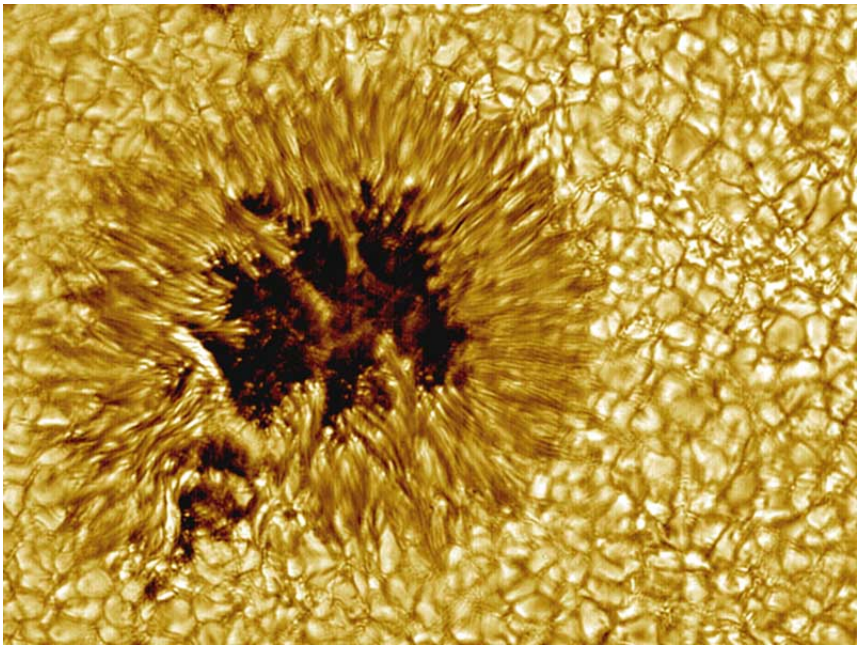

Fig. 1.2.: Sunspot and surrounding solar granulation. Image taken by the VTT (Vacuum Tower Telescope). Credit: VTT, NSO (National Solar Observatory), NOAO (National Optical Astronomy Observatory).

coming from the convection zone below. The typical extension of a granule is about 1500 km with a lifetime of roughly $8 - 20$ minutes (see e.g., Aschwanden, 2019).

The Chromosphere is the next layer where the density further decreases. Although the temperature rises when going up higher and approaching the solar corona, the chromosphere contributes only very little to the total solar radiation. Thus, observation is difficult, but can be done either by observing through very specific wavelength filters (unveiling the chromospheric network, which is formed by magnetic fields) or sometimes in solar eclipses at the edge of the occulting moon. Another feature that can be viewed in this layer of the Sun are plage regions, which appear as bright structures on the solar disk. The chromospheric temperature increase could be explained by heating through either magneto-acoustic waves or Alfvén-waves and turbulence (see e.g., Aschwanden, 2019).

1.1.3 The Solar Corona

The outer atmosphere of the Sun is called the solar corona. Its spectrum has multiple components: a continuum spectrum formed by light originating from the photosphere that scatters off free electrons. The high velocities of those electrons leads to such a strong line broadening that the original absorption line spectrum from the photosphere is transformed into a continuum spectrum. The situation is different if this photospheric light is scattered off dust particles and thus reproduces

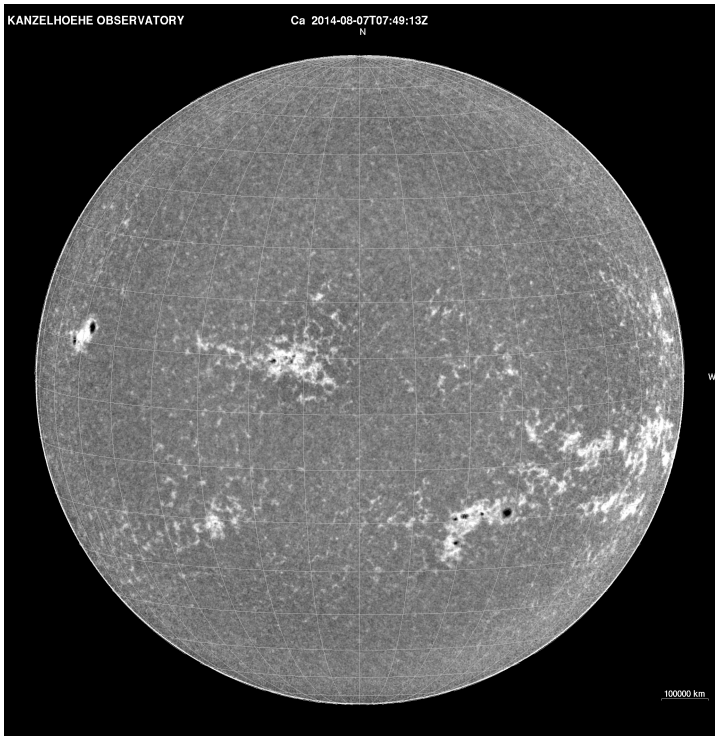

Fig. 1.3.: Contrast enhanced image of the Sun in the Ca II K filter (wavelength: 393.37 nm) on 08-07-2014, including plage regions and the chromospheric network. Image taken from the Kanzelhöhe Observatory.

the Fraunhofer spectrum. Another component is formed by highly ionized elements, leading to an emission spectrum. The scattering process that forms the continuum component is called Thomson scattering and is responsible for what we observe in white-light (the visible part of the spectrum). Electromagnetic radiation is scattered off free electrons that emit light again perpendicular to the incident radiation. While the assumption that the scattering process has its maximum in the plane of sky (the plane perpendicular to the observers line of sight) is approximately true if one observes close to the Sun, deviations occur for increased distances for geometrical reasons (Vourlidas and Howard, 2006). The instrumentation that captures white-light images of the corona are called coronagraphs. Additionally the white-light corona can be captured by imaging solar eclipse events. The EUV (= extreme ultraviolet; $10 - 125$ nm) emission however is formed by highly ionized elements in the corona and can only be observed at lower altitudes compared to white-light images (see e.g., Aschwanden, 2019). The presence of these highly ionized elements (like Fe IX and Fe XII) also gives a hint of the temperature in the corona. With the knowledge about the ion abundance one can then create EUV images using filters that are only transparent for the wavelength of the emitted light from these particles.

1.2 The Coronal Magnetic Field

The Sun also features a dynamic and complex magnetic field that can be measured in the photosphere in the form of magnetograms (using the Zeeman effect). But the magnetic structures actually rise way further than just the surface - they extend up to the corona and the heliosphere (the sphere of influence of the Sun, which includes the whole solar system). The global magnetic field is dependent on the activity phase of the Sun: it is a poloidal-like dipole field in the solar minimum and a toroidal-like dipole field during the maximum phase (see e.g., Aschwanden, 2019). On top of this magnetic field configuration, locations of high magnetic field (originating from sunspots and active regions) are superposed.

The magnetic field can be divided into closed and open structures, which plays an important role in the work related to this thesis. Open magnetic topology means field lines emerging from the surface that seem to leave the Sun completely. Note that following the current theory of electrodynamics, there are no magnetic monopoles (see e.g., Griffiths, 2017), thus magnetic field lines eventually have to turn back to the Sun at some point far away in the heliosphere. Closed magnetic topology means field lines that are closed at reasonable distances near the solar surface, forming loop structures. Open fields can actually be observed in EUV images of the corona: they appear as dark regions called coronal holes. While we have not the best insight into the polar magnetic field because of the line-of-sight problem (see Section 3.4), it seems that the poles are covered by large-scale coronal holes and thus have predominantly open magnetic field. Another prominent large-scale magnetic feature in the solar corona are streamers. These are loop-structures (enveloped by open fields) that form cusp-like tips. There are two types of streamers. On the one hand there are so-called helmet streamers, that form from bipolar regions. On the other hand pseudostreamers are connected to an even amount of bipolar structures and thus their legs have the same polarity (e.g., Cranmer et al., 2017).

Although it is not possible to measure the coronal magnetic field directly, there is the possibility to derive the magnetic structure in the corona via the frozen-in theorem. It states that if one considers the coronal plasma as infinitely conducting electrical fluid, then the magnetic field lines are stuck to the plasma or vice versa - depending on another quantity, called the plasma-beta:

$$\beta = P_{\text{gas}}/P_{\text{magnetic}} = nk_BT/(B^2/2\mu_0)$$

If the gas pressure dominates (i.e. $\beta >> 1$) then the magnetic field has to follow the plasma and if $\beta << 1$, then the magnetic field is dominating the plasma. So,

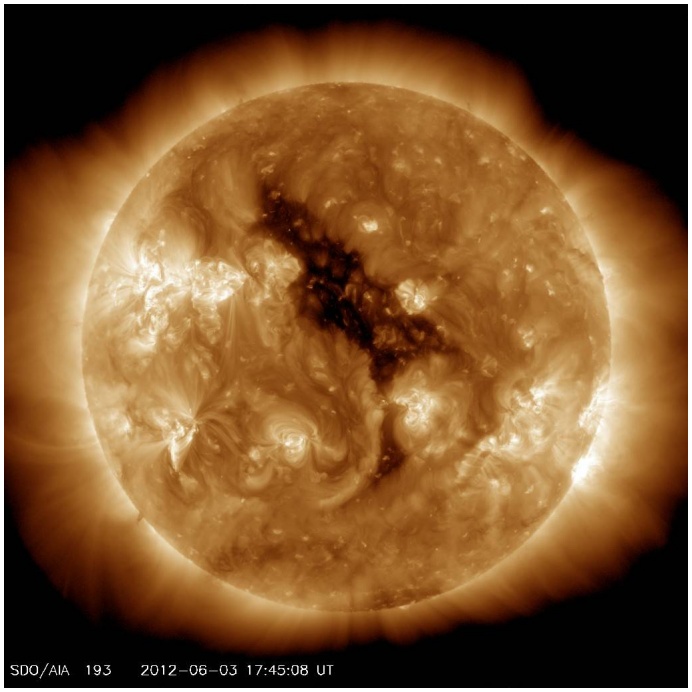

Fig. 1.4.: Coronal hole as observed by the SDO (Solar Dynamics Observatory)/AIA (Atmospheric Imaging Assembly) instrument on 2012-06-03. Image credits: NASA.

the plasma structures that can be seen in white-light images of the corona actually indicate the underlying magnetic field (within the frame of our approximations done, to apply the theorem). In fact, the plasma beta in the solar corona is very small (e.g., Rodríguez Gómez et al., 2019), thus with deriving magnetic field information one can already get a good idea about the plasma density distribution in the corona. This can be seen especially in solar eclipse photographs which already have undergone some image enhancement (see Figure 1.5). Here it is even possible to identify individual field lines.

1.3 Solar Activity

The Sun undergoes an activity cycle altering some of it's important properties, like magnetic field, solar wind outflow, frequency of dynamic processes such as flares and CMEs (= coronal mass ejections), etc. This activity cycle has an approximate duration of 11 years. The relative sunspot number R (also International Sunspot Number), as defined in Section 1.1.2, serves as the prime indicator of solar activity (usually smoothed as 13-months running average). This is mostly because it has the longest history of data availability out of all possible activity indicators, with it being recorded daily since 1849 (Hathaway, 2015). Figure 1.6 shows the solar activity variation as measured by monthly averaged sunspot numbers.

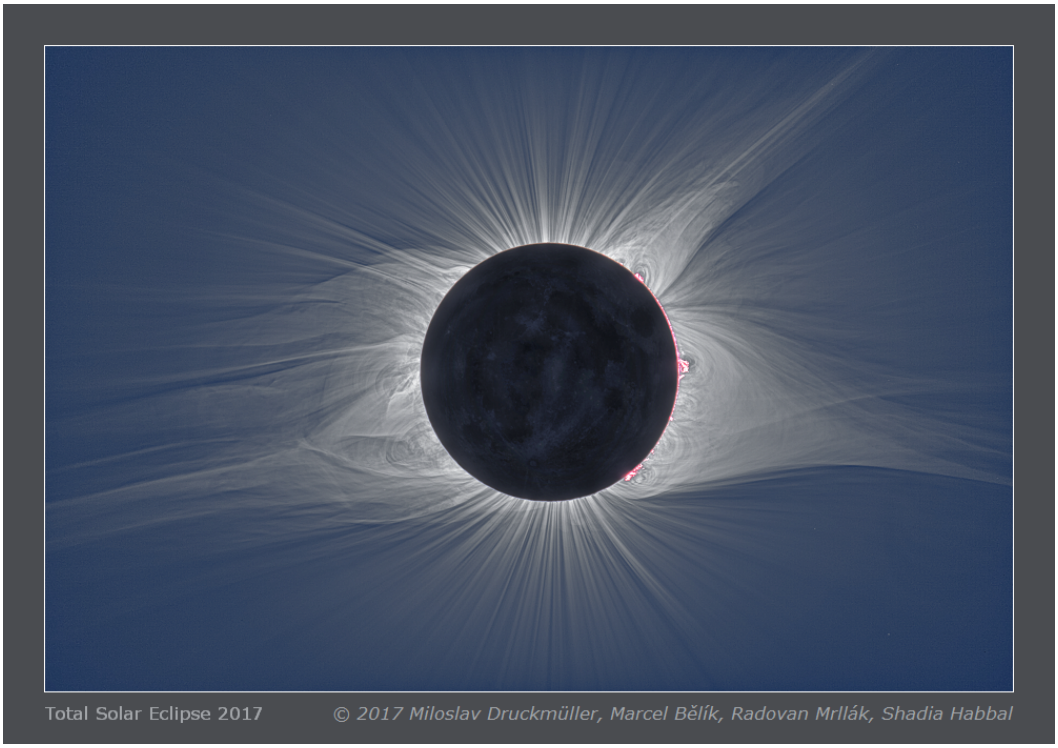

Fig. 1.5.: Enhanced high-resolution image for the solar eclipse on 08-21-2017. Image Credits: Miloslav Druckmüller, Marcel Bělík, Radovan Mrllák, Shadia Habbal

The distribution of magnetic flux on the solar surface varies with the activity phase. In the minimum (i.e., in the beginning of a new cycle) most flux is located at the poles. North and South poles have different polarities. Soon new flux is created at latitudes of ± 30 degrees forming sunspots and bipolar regions, which progressively evolve towards the equator with the duration of the solar cycle (e.g., Mackay and Yeates, 2012). Additionally, the magnetic surface flux follows two laws: 1) Hale's law and 2) Joy's law. Hale's law states that when bipolar fields emerge, the leading polarity (i.e., the polarity of the part of the structure that faces the rotation direction) is the same as the polarity of the polar flux of the hemisphere it is located in (Hale and Nicholson, 1925). Joy's law states that the leading spot is located closer to the equator than the following spot of a bipolar group. Furthermore, the tilt angle seems to be latitude dependent: The closer the group is to the equator, the smaller the tilt angle (Hale et al., 1919). Towards the end of a cycle the main magnetic polarity, as given by the polar fields turns around due to meridional flows transporting following flux from bipolar regions to the poles, while the leading polarity spots tends to cancel with those of the opposing hemisphere at the equator (Mackay and Yeates, 2012). With that a new minimum is initiated, preparing the start of a new cycle. Thus, the magnetic solar cycle lasts twice as long as the sunspot cycle (i.e., 22 years, see Mackay and Yeates, 2012). The evolution of magnetic fields is illustrated in Figure 1.7.

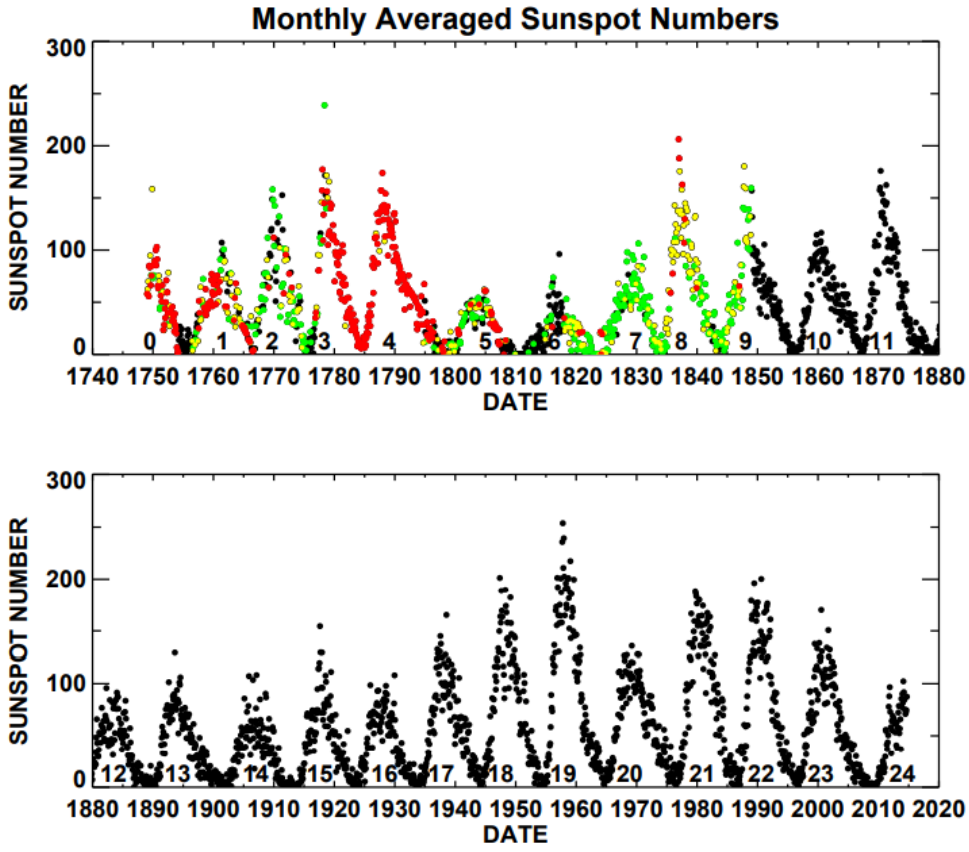

Fig. 1.6.: Monthly averaged sunspot numbers, where black indicates daily recording of sunspot numbers while green indicates 1 to 10 days missing observations, yellow 11 to 20 days missing and red shows more than 20 days missing observations. Figure taken from Hathaway (2015).

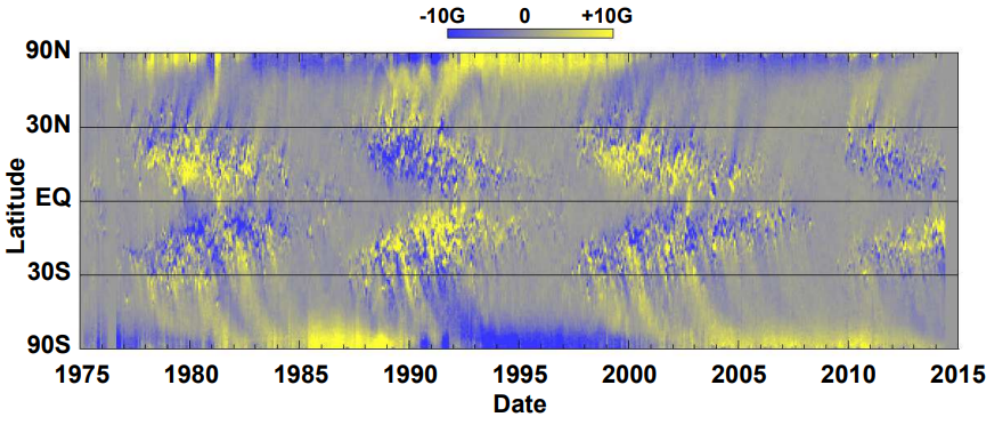

Fig. 1.7.: Magnetic "Butterfly" Diagram showing the movement of magnetic polarities with time using longitudinally averaged radial magnetic field (data from Kitt Peak and SOHO). The image is taken from Hathaway (2015).

1.4 The Solar Wind

Because the Sun is not a static closed system, there are a lot of dynamic processes happening on its surface. It is not only energy that flows out of the system in the form of heat and radiation - there is also a mass flux in the form of particles that leave the Sun constantly. This particle stream is called the solar wind. Though there is a constant flux from the Sun, it is not homogeneous. There are two main components, being the slow and the fast solar wind streams. But it is not only the wind speeds, with 250−450 km/s and 450−800 km/s respectively, that differ between the two types: also various properties e.g. ion-composition or particle density of the flows are significantly different (Cranmer et al., 2017). The fast component originates from coronal holes, while for the slow component of the solar wind, the origins are not entirely clear (e.g., Aschwanden, 2019). Because there are two kinds of streams, naturally compressions, rarefactions and shocks can form in regions where they collide. These are called stream interaction regions (SIR's) or if they last over multiple rotations co-rotating interaction regions (CIR's). It is important to investigate such structures because they can significantly impact the Earth's iono- and thermosphere and thus influence spacecraft orbits (e.g., Cranmer et al., 2017). While the solar wind flows out radially, the solar wind structure in interplanetary space forms the so-called Parker Spiral because of the solar rotation. At the regions where the magnetic field changes it's polarity, a thin separation layer containing electric currents forms. This region is called the heliospheric current sheet and is shaped by the Parker Spiral and the magnetic field. The current sheet is rather plane-like in the solar minimum phase, while it has a warped "spinning ballerina skirt"-like structure in more active phases (see e.g., Schwenn, 2006).

1.5 Space Weather

Space Weather is used as a term, collecting the impact of various processes at the Sun on Earth. Technology, be it space-borne or ground-based, as well as our own health and life can be heavily affected. The geomagnetic impacts can be dramatic enough that they lead to problems in our power distribution networks, which is tied to big economic costs (Eastwood et al., 2018). The most notable events that can cause such harms are solar flares and CME's as well as solar energetic particles (SEP's). Flares are sudden flashes on the solar surface that are connected to strong radiation. The radiation itself covers a variety of wavelengths. Elevated levels of X-ray and EUV emission can cause various effects on our Earth's atmosphere (e.g., heating) and therefore change orbits of important spacecrafts (e.g., Hathaway, 2015). The energy that is released in such an event also varies greatly, between 10^{19} J to 10^{25} J, where the non-radiative portion is released in the form of heating and

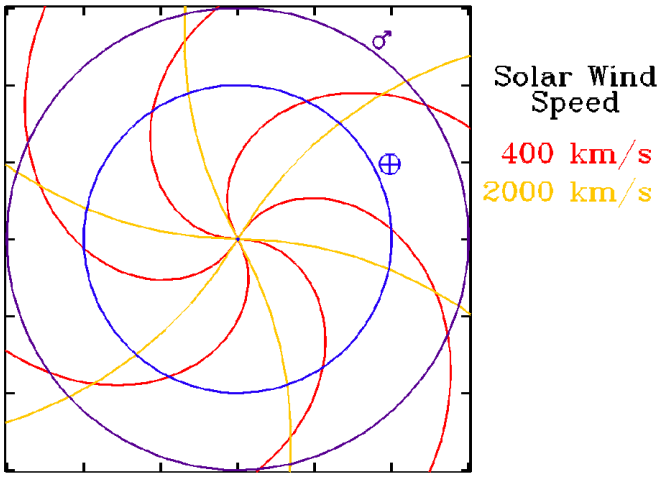

Fig. 1.8.: Parker Spiral structure in the heliosphere for two different wind speed components. Image credit: NASA.

acceleration of particles (e.g., Schwenn, 2006). A flare may not strictly be associated with geoeffectiveness, different to CME's hitting the Earth. Here causal links between observed shocks and CMEs can be established (e.g., Schwenn, 2006).

CMEs are (as the name suggests) clouds of ionized solar material being ejected from the surface and travel through interplanetary space. They are the most geoeffective events, i.e., have the biggest impact on our Earth. On their way from Sun to Earth they don't remain constant though. Significant changes in their kinematic behaviour during their propagation through interplanetary space can occur, based on the underlying solar wind structure (Temmer et al., 2011). CME properties in general are subject to great variation. CME speeds can go up to almost 3000km/s, the angular width average at around 50 degrees. Masses range in between 10^{13}g and 10^{16}g and energies roughly vary from 10^{27}erg to 10^{33}erg (Schwenn, 2006; Temmer, 2021).

SEP's are particles coming from the Sun reaching near-relativistic energies. They originate from flares as well as coronal and interplanetary shock waves (Schwenn, 2006). Because of their large speeds they can reach Earth very fast (roughly an hour after their acceleration) and cause harm to sensitive instruments of a spacecraft. The acceleration mechanism of SEPs as well as their forecasting is still an issue. It seems though that the complexity of the underlying active region has a notable contribution to the likelihood of SEP events, preferring big bipolar regions with large asymmetric penumbrae and small additional surrounding spots (e.g., Bronarska and Michalek, 2017).

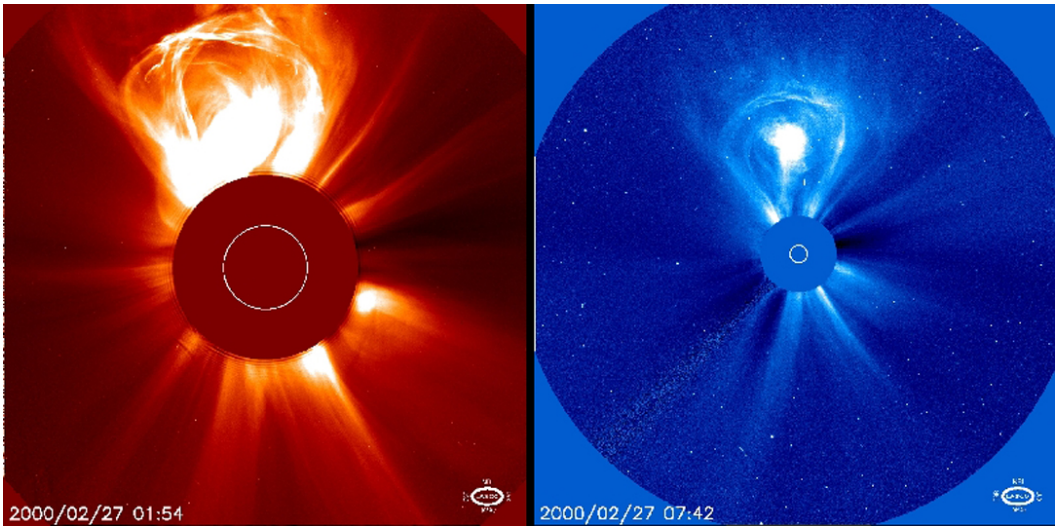

Fig. 1.9.: Coronal Mass Ejection observed by the SOHO (Solar and Heliospheric Observatory)/LASCO (Large Angle and Spectrometric Coronagraph) C2 (left) and C3 (right) instruments on 02-27-2000. Image credits: SOHO ESA and NASA.

Since all of these geoeffective phenomena are linked to the Sun's magnetic behavior, it is important to understand how to correctly model the solar magnetic field to enable reliable space weather predictions. Furthermore, the solar wind influences propagational evolution of CMEs and thus accurate background solar wind modelling is necessary as well.

2 Models

2.1 PFSS Model

One commonly used magnetic field model for the solar corona is the so-called Potential Field Source Surface (short: PFSS) model. Its basic assumptions are that the corona is completely free of currents and time steady. By having a look at the Maxwell equations one notices that with these assumptions the rotation of the magnetic field $\boldsymbol{B}$ vanishes. This means that the $\boldsymbol{B}$-field can be calculated from a scalar potential ψ (in contrast to the classical vector potential), where the potential can be simply calculated from a Laplacian equation (see e.g., Mackay and Yeates, 2012):

$$\nabla \times \boldsymbol{B} = 0 \Rightarrow \boldsymbol{B} = -\nabla\psi \Rightarrow \Delta\psi = 0$$

On its lower boundary, values from a magnetogram (a magnetic map of the Sun's surface) are used as an input to the model. On the, usually spherical, upper boundary the magnetic field is forced to be radial, so when using spherical coordinates one forces B_θ and B_ϕ to be zero. This boundary layer is called the source surface. Above this source surface the magnetic field lines that reach this height continue to be strictly radial (Mackay and Yeates, 2012). The boundary height for the source surface is not set to a fixed value by physical calculations - in fact it is a somewhat free, empirical choice that has to be made. Usually this height is set to 2.5 solar radii (Riley et al., 2006). This simple choice has big influences though, e.g., on the amount of generated open flux. Choosing a lower lying source surface will generate more open flux compared to higher source surfaces, because more field lines actually reach the surface and are thus forced to be radial and cannot close (see e.g., Asvestari et al., 2019). This can be nicely seen in Figure 2.1.

Computationally the Laplacian equation is typically solved by the use of a spherical harmonics expansion (see e.g., Mackay and Yeates, 2012):

$$\psi(r,\theta,\phi) = \sum_{\mathrm{l}=0}^{\infty} \sum_{\mathrm{m}=-\mathrm{l}}^{+\mathrm{l}} (f_{\mathrm{lm}} r^{l} + g_{\mathrm{lm}} r^{-(l+1)}) P_{\mathrm{l}}^{\mathrm{m}}(cos(\theta)) e^{im\phi}$$

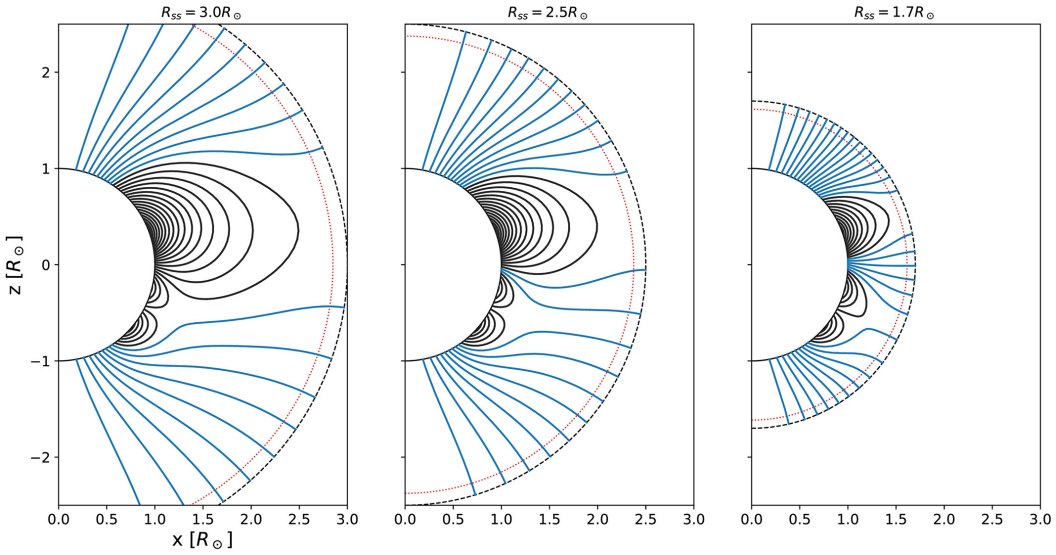

Fig. 2.1.: Open field line topology for different source surface heights by Asvestari et al. (2019).

with $P_{\rm l}^{\rm m}(cos(\theta))$ the associated Legendre polynomials and the coefficients:

$$f_{\rm lm} = -(l{\rm R}_\odot{}^{l-1} + (l+1){\rm R}_\odot{}^{-l-2} R_{\rm ss}^{2l+1})^{-1} b_{\rm lm}$$

$$g_{\rm lm} = -f_{\rm lm} R_{\rm ss}^{2l+1}$$

Here, $\rm R_\odot$ is the solar radius, $R_{\rm ss}$ is the source surface radius and the $b_{\rm lm}$ are the coefficients of the photospheric $B_{\rm r}(r = {\rm R}_\odot, \theta, \phi)$ distribution. The solution for the magnetic field components in spherical coordinates can then be written as (see e.g., Mackay and Yeates, 2012):

$$B_{\rm r}(r,\theta,\phi) = \sum_{\rm l=0}^{\infty} \sum_{\rm m=-l}^{+l} b_{\rm lm} c_{\rm l}(r) P_{\rm l}^{\rm m}(cos(\theta)) e^{im\phi}$$

$$B_{\rm \theta}(r,\theta,\phi) = -\sum_{\rm l=0}^{\infty} \sum_{\rm m=-l}^{+l} b_{\rm lm} d_{\rm l}(r) \frac{dP_{\rm l}^{\rm m}(cos(\theta))}{d\theta} e^{im\phi}$$

$$B_{\rm \phi}(r,\theta,\phi) = -\sum_{\rm l=0}^{\infty} \sum_{\rm m=-l}^{+l} \frac{im}{sin(\theta)} b_{\rm lm} d_{\rm l}(r) P_{\rm l}^{\rm m}(cos(\theta)) e^{im\phi}$$

with

$$c_{\rm l}(r) = \left(\frac{r}{\rm R_\odot}\right)^{-l-2} \left(\frac{l+1+l(r/R_{\rm ss})^{2l+1}}{l+1+l({\rm R_\odot}/R_{\rm ss})^{2l+1}}\right)$$

$$d_{\mathrm{l}}(r) = \left(\frac{r}{\mathrm{R}_\odot}\right)^{-l-2} \left(\frac{1 - l(r/R_{\mathrm{ss}})^{2l+1}}{l + 1 + l(\mathrm{R}_\odot/R_{\mathrm{ss}})^{2l+1}}\right).$$

The big advantage of PFSS model implementations is that they are comparatively cheap to run in terms of computational resources. Its pitfalls lie in the assumptions, because neither is the coronal magnetic field static (this assumption especially makes it impossible to model magnetic reconnection, which is a highly dynamic phenomenon), nor is it completely current free. It was shown though, that the resulting field configuration still captures the global magnetic field topology quite well in comparison to more complex methods such as magnetohydrodynamic (short: MHD) implementations, as long as non-potential effects (such as magnetic reconnection) are not the main focus or contributor to the magnetic fields (Riley et al., 2006). This is quite well satisfied during solar minimum phases for example, or in certain sub-regions of lower activity. A small showcase of such a model's output and comparison can be viewed in figure 2.2.

2.2 SCS Model

To improve the PFSS model, Schatten in 1971 introduced the Schatten Current Sheet (short: SCS) model. It deals with the problems of the current-free assumption and the unrealistic purely radial nature of the field lines above the source surface (Schatten, 1971). This model modifies an already-calculated PFSS result by first introducing an intermediate boundary surface at the so-called Schatten current sheet height, originally located at 1.6 $\mathrm{R}_\odot$ (Schatten, 1971). However, this boundary radius is nowadays handled as a free parameter and subject to investigations (as carried out in the frame of this thesis) to find the ideal height. The $\boldsymbol{B}$-field then gets re-oriented such that B_{r} is always > 0 there (so the signs of all components get reversed, if $B_{\mathrm{r}} < 0$), thus temporarily violating $\nabla \cdot \boldsymbol{B} = 0$ on the boundary surface. Then the field above the SCS height is calculated by using the potential field solution, but matching the lower boundary values to the values of the re-oriented field components at this surface. In the last step the re-oriented field is reversed again to restore the originally calculated configuration on the interior, which creates currents in the outer parts at locations where B_{r} is low (see e.g., Mackay and Yeates, 2012). Those currents form thin current sheets that separate magnetic regions of opposite polarity (Schatten, 1971).

With the inserted currents the final result will introduce a bending of the field lines and thus a more realistic magnetic field configuration, especially at larger

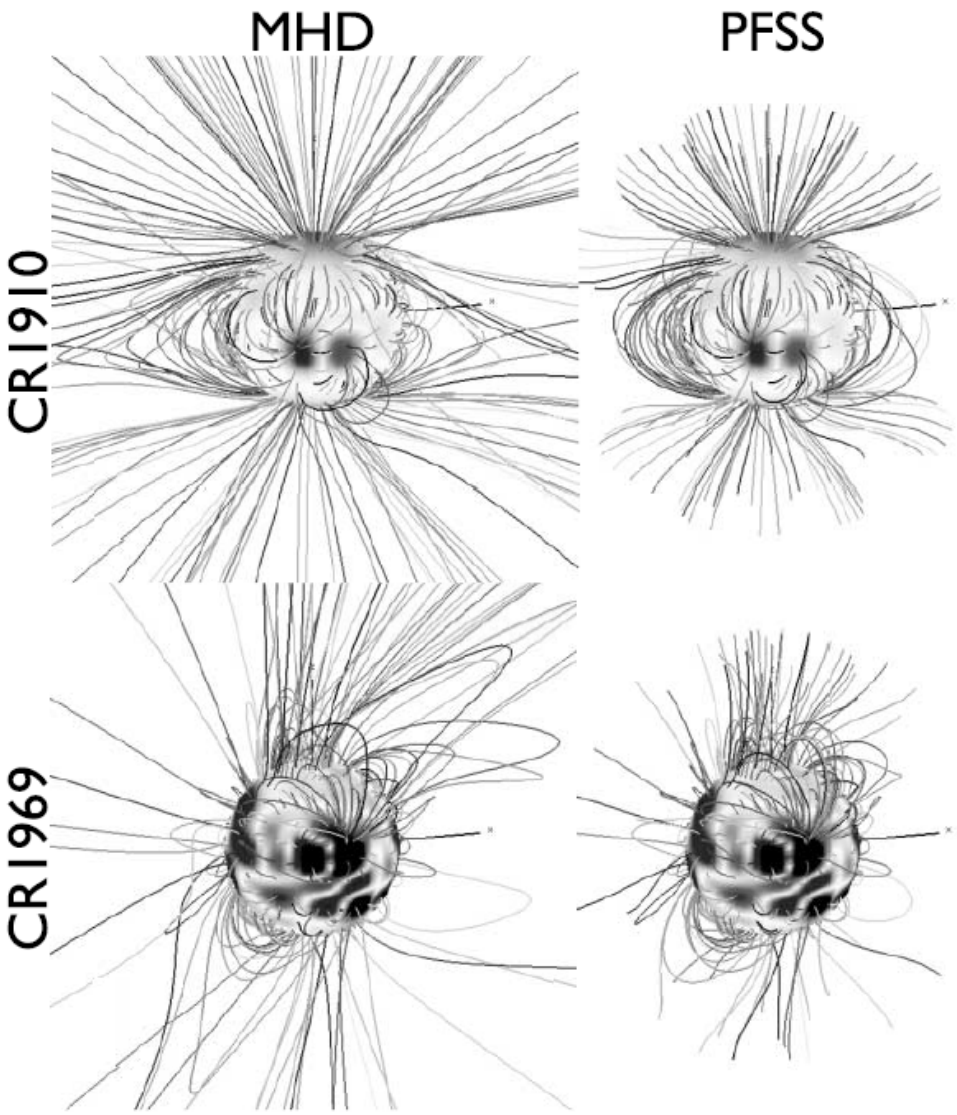

Fig. 2.2.: Comparison between MHD (left) and PFSS model (right) from Riley et al. (2006).

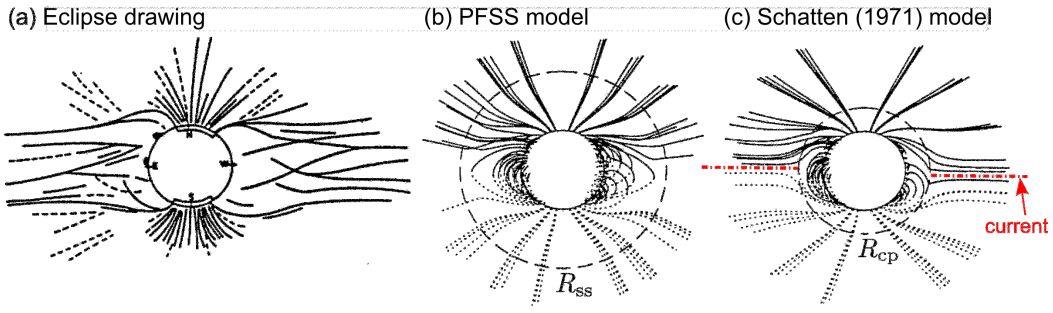

Fig. 2.3.: Conceptual drawings from Zhao and Hoeksema (1994), adapted by Mackay and Yeates (2012), of a) a solar eclipse, b) a standard PFSS model c) the SCS enhancement with the current sheets shown. R_{ss} marks the source surface height and R_{cp} the SCS height.

distances from the Sun (Mackay and Yeates, 2012). This is shown in a drawing in Figure 2.3. The transition between the two model regions (the inner PFSS domain and the outer SCS domain) is not smooth (because of different types of boundary conditions) and thus it is conventional to set the SCS boundary height below the PFSS boundary height, with suggested values of $R_{\mathrm{ss}} = 2.6\mathrm{R}_{\odot}$ and $R_{\mathrm{scs}} = 2.3\mathrm{R}_{\odot}$ (EUHFORIA default values, see Pomoell and Poedts, 2018, and Section 2.5). Similar as in the discussion of the PFSS boundary height in Section 2.1 the SCS boundary height is a free parameter - therefore making it a set of two free parameters for the whole coronal magnetic field model. As already pointed out, the exact values are subject to investigations and one of the main goals of this work is to test different parameter sets and compare the results with observational data (see later in Section 3).

2.3 WSA Model

The Wang-Sheeley-Arge (short: WSA) model is an empirical mathematical model to predict the solar wind speed at Earth (Arge et al., 2003). Originally the model would use a PFSS model and introduce a parameter called the flux tube expansion factor f and the solar wind speed v_{sw} at Earth, where f is given by:

$$f = \left(\frac{\mathrm{R}_{\odot}}{R_{\mathrm{ss}}}\right)^2 \left(\frac{B(\mathrm{R}_{\odot})}{B(R_{\mathrm{ss}})}\right).$$

where R_{ss} denotes the source surface radius from the PFSS model and B is the total magnetic field strength (Wang and Sheeley, 1990). This value f can be thought of as the expansion of a photospheric flux tube at the source surface in comparison to purely radial expansion (Arge et al., 2003). This factor was then set in relation to the solar wind speed Earth (Wang and Sheeley, 1990). An improvement was found when incorporating the minimal angular distance θ of the footpoint of an open field line with the nearest coronal hole boundary. This lead to the WSA model with the following relation for the solar wind speed (Arge et al., 2003):

$$v_{\mathrm{sw}}(f,\theta) = 265 + \frac{25}{f^{2/7}}\left(5 - 1.1e^{1-(\theta/4)^2}\right)^2 \mathrm{km/s}$$

For space weather forecasting purposes the WSA model's PFSS is often improved by using an SCS model, because it produces more accurate results, especially at larger radii (Mackay and Yeates, 2012).

2.4 Magnetohydrodynamics

Magnetohydrodynamics (in short: MHD) is, as the name suggests, the unification of electrodynamics and hydrodynamics to describe magnetized fluids. This is especially useful for plasma physics as in most cases MHD gives a very good mathematical description of plasma. As the Sun and the solar wind consists of ionized particles (i.e., plasma) the MHD approach is a useful tool for simulations in solar physics (see e.g., Mackay and Yeates, 2012). It has to be noted though, that it is only applicable for large-scale and low frequency phenomena (Lionello et al., 2009). The electrodynamic fundamentals are rooted in the so-called Maxwell equations, which are given in the following (Griffiths, 2017):

$$\nabla \cdot \boldsymbol{E} = \frac{\rho}{\epsilon_0}$$
$$\nabla \cdot \boldsymbol{B} = 0$$
$$\nabla \times \boldsymbol{E} = -\frac{\partial \boldsymbol{B}}{\partial t}$$
$$\nabla \times \boldsymbol{B} = \mu_0 \boldsymbol{J} + \mu_0 \epsilon_0 \frac{\partial \boldsymbol{E}}{\partial t}$$

$\boldsymbol{E}$ is the electric field, ρ the charge density, ϵ_0 the vacuum permittivity, $\boldsymbol{B}$ the magnetic flux density, t the time, μ_0 the vacuum permeability and $\boldsymbol{J}$ the current density. The first equation states the existence of sources and sinks of the electric field, while the second equation negates the existence of such for magnetic fields. Thus, there are no magnetic monopoles. The other two equations state for example that changing electric fields induce a magnetic field and vice-versa. To extend these equations in the MHD context, usually the equation of continuity and equation of motion originating from hydrodynamics are added, as well as Ohm's law and an energy balance. To combine both electrodynamics and hydrodynamics, some adjustments have to be made to make them compatible (e.g., neglecting the $\frac{\partial \boldsymbol{E}}{\partial t}$ term in the last equation). Because there are different possibilities of what kind of terms to include (e.g., gravitational terms in the equation of motion, different energy transfer models, etc.), many different formulations of these equations can be made. An example of a set of MHD equations from the "Bifrost" code are shown in the following (Gudiksen et al., 2011):

$$\frac{\partial \rho_m}{\partial t} = -\nabla \cdot \rho_m \boldsymbol{u} \tag{2.1}$$

$$\frac{\partial \rho_m \boldsymbol{u}}{\partial t} = -\nabla \cdot (\rho_m \boldsymbol{u}\boldsymbol{u} - \tau) - \nabla P + \boldsymbol{J} \times \boldsymbol{B} + \rho_m \boldsymbol{g} \tag{2.2}$$

$$\frac{\partial \boldsymbol{B}}{\partial t} = -\nabla \times \boldsymbol{E} \tag{2.3}$$

$$\mu_0 \boldsymbol{J} = \nabla \times \boldsymbol{B} \tag{2.4}$$

$$\boldsymbol{E} = \eta \boldsymbol{J} - \boldsymbol{u} \times \boldsymbol{B} \tag{2.5}$$

$$\frac{\partial e}{\partial t} = -\nabla \cdot e\boldsymbol{u} - P\nabla \cdot \boldsymbol{u} + Q \tag{2.6}$$

Here, ρ_m is the mass density, $\boldsymbol{u}$ the velocity, τ the stress tensor, P the pressure, $\boldsymbol{g}$ the gravitational acceleration, η the magnetic diffusivity and e the energy per unit volume. Q includes various heating and cooling terms. Equations 2.1 and 2.2 originate from hydrodynamics and are called the continuity equation and equation of motion, respectively. While equations 2.3, 2.4 as well as Ohm's law (2.5) make up the electrodynamic part of the set, equation 2.6 provides some kind of closure of the system through energy balance. An advantage of the MHD formulation is that it can not only successfully model the solar atmosphere, but also enables solar wind modelling with extending the model domain to the heliosphere (see e.g., Mackay and Yeates, 2012), which is also part of the space weather simulation code used in the frame of this thesis' work (see Section 2.5.2, where also another a set of possible MHD equations is given).

Often a distinction between ideal and resistive MHD is made. The ideal case deals with highly conducting plasma and thus approximates the conductivity to approach infinity. Thus, η in equation 2.5 becomes 0. In this formulation there is no possibility of the occurance of magnetic reconnection processes, which is different in the resistive case, where the conductivity is finite.

2.5 EUHFORIA

Because of the big socioeconomic impact that a variety of space weather events can have (as discussed in Chapter 1.5) it became crucial to have forecasting tools to predict such events. One of those tools is EUHFORIA, (EUropean Heliospheric FORcasting Information Asset), which is a Python-based simulation code (Pomoell and Poedts, 2018). Its spatial structure is split into two domains: the coronal domain and the heliospheric domain. The coronal domain starts from the solar surface up to

0.1 AU, and the heliospheric domain extends from this 0.1 AU-boundary up to your point of interest (e.g. 2 AU).

2.5.1 The Coronal Domain

As observational input initiating the simulation, a synoptic magnetogram of the Sun is needed. This magnetogram is then used in the coronal domain to compute the magnetic field configuration from a PFSS model. This PFSS solution is then used to compute an SCS model to further improve the result for the magnetic field structure (for details, see Sections 2.1 and 2.2). In comparison to the solution for the PFSS model given in section 2.1 the Laplacian equations for both PFSS and SCS are solved using solid harmonics, with the default order of expansion of 120 for the PFSS and 70 for the SCS model (Pomoell and Poedts, 2018).

For the solar wind conditions at the boundary of 0.1 AU distance from the Sun a modified WSA model (see Section 2.3) for the solar wind speed is used. Since the WSA model's original purpose was to predict the solar wind speed at Earth (Arge et al., 2003), a modification to give the resulting speed at the border of the coronal domain at 0.1 AU has been made (though the exact model function is left open to the modeller). One big difference to the original approach is that for the flux tube expansion factor, instead of using the total magnetic field ratio, only the radial magnetic field is used, due to the horizontal component at the photospheric footpoints being non-negligible (compare with the formula for f in Section 2.3). The other parameters necessary for the MHD model in the heliospheric domain, being the radial magnetic field B_r, the density ρ and the temperature T, are computed based on the derived wind speed (Pomoell and Poedts, 2018):

$$B_\mathrm{r} = sgn(B_\mathrm{cor}) B_\mathrm{fsw} \left(\frac{v_\mathrm{r}}{v_\mathrm{fsw}} \right)$$

$$\rho = \rho_\mathrm{fsw} \left(\frac{v_\mathrm{fsw}}{v} \right)^2$$

$$T = T_\mathrm{fsw} \left(\frac{\rho_\mathrm{fsw}}{\rho} \right)$$

Here, B_cor is the magnetic field, as derived from the coronal model. The subscript "fsw" means "fast solar wind" and refers to the corresponding typical values for B, ρ and T. One also has to note that the wind speed map is rotated by $10°$ to take the solar rotation into account[1]. The meridional B-field component is set to zero and

[1] The coronal magnetic field model is static and does not simulate the solar rotation. To match the solar wind profile at the boundary of the domain, this $10°$ rotation is necessary.

the azimuthal component is set in such a way to produce no electrical field in the corotating frame of the MHD computation in the heliospheric domain (Pomoell and Poedts, 2018).

2.5.2 The Heliospheric Domain

The plasma parameters at the boundary of the coronal domain computations are then propagated outwards, using ideal MHD in combination with gravity terms (Pomoell and Poedts, 2018):

$$\frac{\partial \rho}{\partial t} = -\nabla \cdot (\rho \boldsymbol{v})$$

$$\frac{\partial \rho \boldsymbol{v}}{\partial t} = -\nabla \cdot \left(\rho \boldsymbol{v}\boldsymbol{v} + \left(P + \frac{B^2}{2\mu_0} \right) - \frac{\boldsymbol{B}\boldsymbol{B}}{\mu_0} \right) + \rho \boldsymbol{g}$$

$$\frac{\partial \boldsymbol{B}}{\partial t} = \nabla \times (\boldsymbol{v} \times \boldsymbol{B})$$

$$\frac{\partial E}{\partial t} = -\nabla \cdot \left(\left(E + P - \frac{B^2}{2\mu_0} \right) \boldsymbol{v} + \frac{1}{\mu_0} (\boldsymbol{B} \times (\boldsymbol{v} \times \boldsymbol{B})) \right) + \rho \boldsymbol{v} \cdot \boldsymbol{g}$$

with:

$$E = \frac{P}{\gamma - 1} + \frac{\rho v^2}{2} + \frac{B^2}{2\mu_0}$$

and

$$\boldsymbol{g} = -\frac{GM_\odot}{r^2} \boldsymbol{e}_r$$

where ρ denotes the mass density, t the time, $\boldsymbol{v}$ the velocity, $\boldsymbol{B}$ the magnetic field, E is the total energy density, P the thermal plasma pressure and G the gravitational constant and γ the polytropic index (which is set to 1.5). G has a value of $(6.67408 \pm 0.00031) 10^{-11} \frac{\mathrm{m}^3}{\mathrm{kg\ s}^2}$ (Mohr et al., 2016).

The equations are solved in the Heliocentric Earth Equatorial (short: HEEQ) frame. The HEEQ frame is a 3D solar coordinate system with the Sun in its center, where the XY-plane is the plane of the solar equator and positive X-direction pierces through the solar equator-solar central meridian line intersection at the given date (Fränz and Harper, 2002). The MHD equations are then numerically solved using a finite volume method in combination with a constrained transport approach (Pomoell and Poedts, 2018). Additionally CME models can be inserted in the heliospheric domain, which is a crucial part for forecasting.

Typically a run of the heliospheric domain can be structured into 3 steps: In the first step the solar wind goes through a relaxation phase in order to generate a steady-state flow, which takes per default 14 simulated days. Since the presence of CMEs changes the background environment significantly, the last 5 days before the start of the forecast are used to insert CMEs from that time to enhance the accuracy of the solar wind environment for the forecast. Together this makes 19 simulated days of preparation. The final step is then the actual forecast (with the starting time being the time the input magnetogram is taken) and can be reasonably run for about 5-7 simulated days (Pomoell and Poedts, 2018).

3 Methodology and Data

With having provided a short introduction to the concept of space weather modelling and especially the EUHFORIA code, the ultimate goal of this work is to investigate the coronal magnetic field model's performance and to find an ideal parameter set. In order to assess the quality of the generated output, observational data for comparison is required. In this chapter the used data and methods are described.

3.1 Selection of Simulation Date

As a first step suitable dates for the simulations had to be chosen. One important aspect for choosing a simulation date is of course the state of the Sun at this particular time. Since the PFSS model is time-steady (see Section 2.1) it is best applied in phases of low solar activity. Here, dynamic processes which are problematic for the PFSS model, are occurring less frequent. Another factor that comes into play is the availability of comparison material for the simulation: one aim was to include solar eclipse images, because of the availability of very well resolved and enhanced photographs that show the white-light corona in great detail. Moreover white-light images in general serve as very good comparison material for magnetic field models since the plasma structures in the corona follow mostly the magnetic field lines (see Section 1.2). The inclusion of solar eclipse images though narrows down the amount of possible dates significantly. Furthermore, it is also of interest to have other suitable white-light images to compare with, for example from coronagraphs, but also EUV maps of the corona. Therefore suitable instrumental data has to be available. In the end the dates 01-Aug-2008, 22-Jul-2009, 11-Jul-2010 and 21-Aug-2017 were chosen, with special focus on the 01-Aug-2008 and 11-Jul-2010. In addition, 19-Jun-2011 and 13-Nov-2012 served as test dates for first investigations of the model's behavior (see Section 4.2).

3.2 White-Light Data

To compare with the white-light corona (see Section 1.1.3) various image sources are used. There are two main types of imaging the white-light corona: 1) Through so-called coronagraphs and 2) through high resolution solar eclipse photography. A

coronagraph is an instrument that blocks out the bright light coming from the solar disk to get a view on the much fainter solar corona (artificial eclipse). In our case we use coronagraph data from two satellite missions: the STEREO (Solar Terrestrial Relations Observatory, Kaiser et al., 2008) twin satellites and the SOHO satellite (Solar and Heliospheric Observatory, Domingo et al., 1995).

The launch of the STEREO spacecraft (STEREO A and STEREO B) was on 26-Oct-2006 and were then subsequently brought into a heliospheric orbit. The uniqueness of this mission comes from the fact that both spacecraft carry identical instruments, but observe the Sun from different locations on the orbit: One is trailing Earth, while the other one is leading (Kaiser et al., 2008). The coronagraphs from both satellites which we use are called COR1 and COR2. The field of view is 1.5 to 4 solar radii for COR1, while COR2 observes from 2.5 up to 15 solar radii (Howard et al., 2008).

Another suite of coronagraph instruments is LASCO (Large Angle and Spectrometric Coronagraph) aboard SOHO. The spacecraft was launched in late 1995 with the purpose of investigating the Sun from the interior up to the solar wind (Domingo et al., 1995). LASCO contains the three coronagraphs C1, C2 and C3 with field of views of 1.1 to 3 solar radii, 1.5 to 6 solar radii and C3 3.7 to 30 solar radii, respectively (Brueckner et al., 1995). For the analysis in Chapter 4 the LASCO C2 coronagraph is used.

The advantage of having STEREO data is that we gain two additional viewpoints and thus not only enhance quality assessment, but also add to the statistics by increasing the sample size for the comparison with the model. Also, together with Earth view data, e.g. SOHO's Coronagraph LASCO, triangulation is possible such that one gets a better idea of the 3D structure of various coronal features. The position of the STEREO spacecraft with respect to the Earth's position on the orbit is not constant though, as the satellites separate each year by 44 to 45 degrees (Kaiser et al., 2008).

Furthermore, another source of coronal white-light data was used in the form of high-resolution solar eclipse images. During these events the strong light from the solar disk is blocked out by the moon. A clear advantage over other image materials is that very detailed density structures can be unveiled in these events. The sharp gradient of coronal brightness makes it necessary to take multiple images with different exposure times, which then have to be aligned. This alignment process is not trivial and influences the final resolution of the image (Druckmüller, 2009). In this work the solar eclipse images provided by Druckmüller are used (`http://www.zam.fme.vutbr.cz/~druck/eclipse/`).

For the STEREO COR1 images NRGF (Normalizing Radial Graded Filter) processing and additional contrast enhancement was applied to improve the visibility of streamers further away from the Sun (for details see Section 3.3). Moreover, images within a 20 minute window were selected and processed. To minimize short-lived structures and singular image distortions the NRGF images are then stacked. No such procedures were applied for the LASCO C2 data as visibility of features and general contrast were sufficient for the analysis.

3.3 Normalizing Radial Graded Filter (NRGF)

The light that we obtain from the coronal plasma is not only depending on the magnetic field, but also on the plasma density. The plasma density however drops strongly with radial distance to the Sun. Therefore unprocessed coronagraph images suffer from the effect that at quite small radial distances from the Sun's surface, several features are just barely visible (if visible at all). To get most information out of these images it is important to have a proper image processing routine to deal with this problem (similar to multi-exposure time images that are combined to a full solar eclipse image). One of those routines is the so-called Normalizing Radial Graded Filter (short: NRGF). Here the off-limb parts of the image are divided into rings around the Sun. Each ring's brightness gets normalized to its standard deviation - therefore enhancing the weaker outer parts of the image, where the standard deviation should drop. In more detail, the newly calculated intensity value, I' for each pixel is then given as (Morgan et al., 2006):

$$I'(r,\phi) = [I(r,\phi) - I(r)_{<\phi>}]/\sigma(r)_{<\phi>}$$

In the programming language IDL (Interactive Data Language) there exists within the SSW (Solar SoftWare) package a ready-made NRGF routine, where customization can be applied. There is also the possibility of an NRGF-processing via the CORIMP.pro interface - both are shown applied on STEREO A COR1 data for the date 01-Aug-2008 in Figure 3.1, together with the raw COR1 image as well as pre-contrast enhancement. For the regular NRGF routine 15 images from consecutive time steps in COR1's data set were created and then added up (cf. Section 3.2).

3.4 Magnetograms

A magnetogram is a magnetic map of the solar surface. In our case they are essential because these maps serve as input to the magnetic field model (cf. Section 2.1).

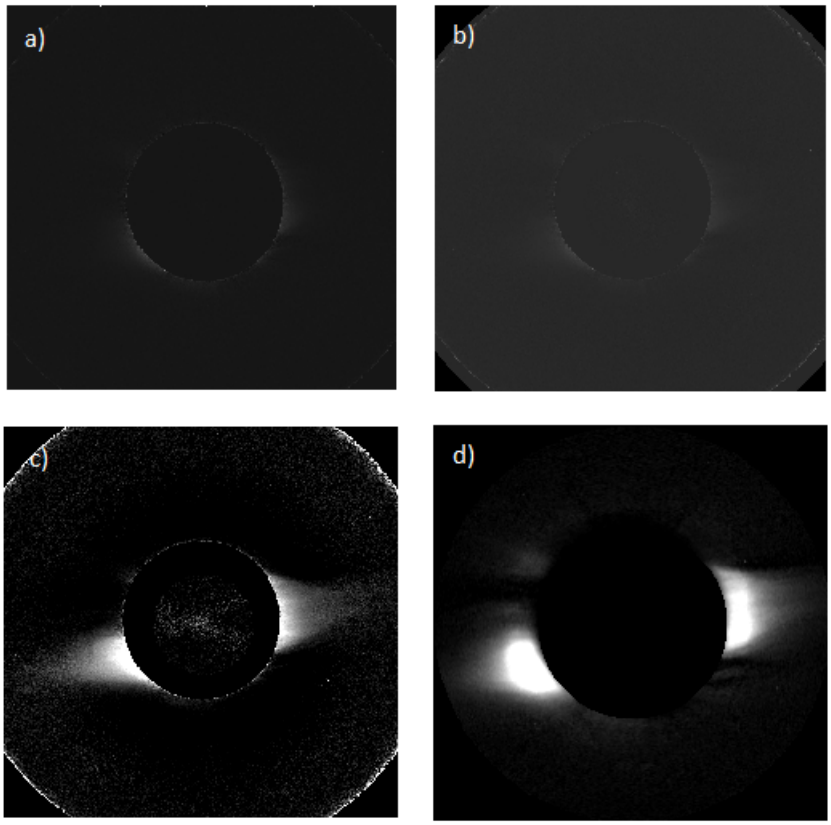

Fig. 3.1.: NRGF showcase for STEREO A's COR1 from the 01-Aug-2008. In panel a) one can see an original STEREO A COR1 image, in panel b) the raw NRGF-processed image, in c) the contrast enhanced final NRGF result as a stack-image of 15 consecutive NRGF images, and in d) the result of the NRGF enhancement from the SSWIDL CORIMP.pro routine.

They are recorded from daily visible disk measurements that are stacked with data from multiple days to create a full-disk magnetic map of the Sun. While full-surface maps are useful and necessary for modelling, they come with certain downfalls. The problem is that one has more than 13 days old data mixed into the same magnetogram together with actual data due to the synoptic nature (Arge et al., 2010). Additionally, as with most photospheric measurements, one has to deal with the line-of-sight problem: The line-of-sight under which we are observing the Sun's polar regions becomes increasingly parallel to the surface tangent. Thus, resolution at these latitudes suffers and moreover the line-of-sight component can not be measured fully. Therefore, results above $\pm$ 60 degrees latitude are problematic.

To deal with the problem of having data from previous days in the magnetogram, magnetic flux transport models are used to give the large-scale temporal evolution of the global magnetic field at the photosphere (Mackay and Yeates, 2012). Here, the old data doesn't stay static but undergoes a time-evolution which is based on physical processes, such as the transport of the magnetic fields through various surface flows. One popular flux transport model is the ADAPT flux transport model, which is based on the Worden and Harvey model (Arge et al., 2010).

For the analysis magnetograms from GONG (Global Oscillation Network Group, Harvey et al. (1996)), MWO (Mount Wilson Observatory) and SDO/HMI (Helioseismic and Magnetic Imager) are used and investigated.

3.5 EUV data

For the quality assessment EUV images serve as additional observational data with which one can compare. They can provide insight on the topology of the magnetic field configuration on the Sun. Here the 195 Å channel of the EIT (Extreme ultraviolet Imaging Telescope) instrument from the SOHO satellite is used. This wavelength filter has a peak temperature of 1.6×10^6 K and corresponds to the EUV emission of the Fe XII ion (Delaboudinière et al., 1995). Furthermore EUV data from the SDO (Solar Dynamics Observatory) satellite mission is used, which was launched on 11-Feb-2010 (Pesnell et al., 2012). In particular, the 193 Å wavelength channel of the AIA (Atmospheric Imaging Assembly) instrument was used, which corresponds to the emission of the Fe XII and Fe XXVI ions (Lemen et al., 2012).

Because the analysis of magnetic topology focuses on the full 360 degrees magnetic on-disk configuration, synoptic EUV maps of the solar surface were needed. The term synoptic means that to get the whole solar disk mapped, one has to fuse multiple images, taken at different phases of the solar rotation. The used Carrington maps

originate from Hess Webber et al. (2014) and Karna et al. (2014) for SOHO/EIT and SDO/AIA, respectively.

For further investigation and testing purposes EUV data from the PROBA2 (Project for Onboard Autonomy 2) spacecraft are also included. This satellite hosts the SWAP (Sun Watcher with Active Pixels and Image Processing) instrument, which has a 174 Å-centered band-pass (Seaton et al., 2013). A nice feature of this mission is the possibility to produce so-called mosaic images from SWAP data. Here, images taken by off-pointing from the center are combined into one image that can show various coronal structures in EUV (Seaton et al., 2013).

3.6 Visualization of the Results

After the model is set up and the runs completed, the results have to be visualized to be able to compare to observational image data. Saving the results not only at the outer boundary, but also at every inner height step in the coronal domain makes field line visualizations possible. Note that per default only values at the outer boundary are saved. Furthermore, the field line tracing enables deriving the topology as one can trace where e.g., closed field lines are originating on the surface.

The computed magnetic field data is then visualized in two ways: First a magnetic topology map is created that shows in which regions the magnetic field lines reach the source surface (i.e., are regions of open topology) and which field lines close beneath the source surface (regions of closed topology).

Additionally to these topology maps the field line configuration is visualized in the whole 3D coronal domain. For the visualization itself the python-visualization tool VisIt (Childs et al., 2012) is used. The created field line model is then plotted over white-light images from the coronagraphs COR1 from STEREO A and STEREO B with additional NRGF enhancement (see Section 3.3), as well as over LASCO C2 and enhanced solar eclipse photographs from Druckmüller (see Section 3.2). The resulting topology maps are compared with on-disk EUV data by means of creating a binary open/closed magnetic regions mask. These masks are computed for both the model output and the EUV image data, where for the latter thresholding has been used to derive the mask.

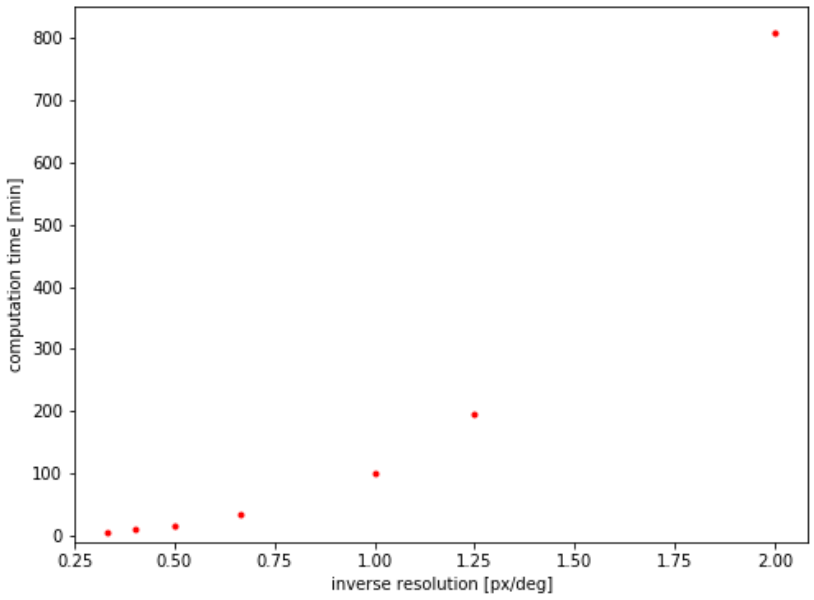

Fig. 3.2.: Computation time in relation to the angular resolution of the model.

3.7 Computational Resources

The coronal model is usually not too computationally expensive, since the PFSS and SCS calculations are rather straightforward for magnetic field extrapolations compared to, e.g., full MHD models (Cranmer et al., 2017). Saving the solution of the computations on the whole 3D-grid is not the standard type of implementation as one is usually only interested in the output at the outer boundary for space weather forecasts. Saving the results on the full 3D-domain increases the necessary resources significantly. From a first testing the computational resources of our local IGAM ("Institut für Geophysik, Astrophysik und Meteorologie") servers proved to be not ideal for the purpose of our work and thus it was decided to use the local high-performance cluster (short: HPC) at Karl-Franzens University (`https://hpc-wiki.uni-graz.at/Wiki-Seiten/Homepage.aspx`). This provided the possibility of running big parts of the at least 67 simulations for the parameter test of one chosen date in parallel. A short test to show the computation time in relation to the chosen angular resolution has been done and can be seen in Figure 3.2. It has to be noted though that the test was performed only once and thus fluctuating activity levels on the cluster are possible sources of errors. The analysis methods that is carried out to assess the model's performance (see Section 4) are all computationally inexpensive and easy to implement.

4 Results

4.1 Set-Up Of The Coronal Domain

For the purpose of this study, the free parameters in the magnetic field model (i.e. the source surface radius R_{ss} and the Schatten current sheet radius R_{scs}) are varied in the following way:

$$R_{\mathrm{scs}}^{\mathrm{ij}} = (1.3 + i * 0.1) R_{\odot}$$
$$R_{\mathrm{ss}}^{\mathrm{ij}} = (R_{\mathrm{scs}}^{ij} + 0.1 + j * 0.3) R_{\odot}$$

with i, j integers (both starting from 0) in such a way that $R_{\mathrm{scs}}^{\mathrm{max}} = 2.8\mathrm{R}_{\odot}$ and $R_{\mathrm{ss}}^{\mathrm{max}} = 3.2\mathrm{R}_{\odot}$, resulting in 67 parameter sets $[R_{\mathrm{scs}}^{\mathrm{ij}}, R_{\mathrm{ss}}^{\mathrm{ij}}]$ (see Table A.1 in A). In contrast to usual runs we are not only interested in the resulting boundary conditions at the outer domain border, but also in the magnetic field configuration inside the coronal model (cf. Section 3.6). To this effect the PFSS+SCS solution is computed and stored at 128 grid points in radial direction. The angular resolution was chosen to be 0.5 degrees per pixel. The order of the solid harmonics expansion to solve the Laplacian equations from the PFSS and the SCS model were both set to be 140.

Additionally to using varying parameter sets, different synoptic input magnetograms are tested. In particular, GONG (Global Oscillations Network Group), GONG ADAPT (ADAPT = Air Force Data Assimilative Photospheric Flux Transport) and HMI (Helioseismic and Magnetic Imager) and MWO (Mount Wilson Observatory) data are used (see Chapter 3). The magnetograms are smoothed to 1 degree per pixel via Gaussian smoothing with a standard deviation of 0.8 degrees per pixel. The test simulations serve the purpose to find out how strong their influence on the result is and which ones produce the most realistic output. Based on the outcomes of this analysis, the best-performing magnetograms are used for the final quality assessment.

4.2 First Results from Test Simulations

As a first step for investigating the EUHFORIA's coronal model and its parameters the date 19-Jun-2011 has been simulated. As it marks the mid-date of the Carrington rotation number 2111, its results are compared with the corresponding EUV Carrington map as well as the white-light data from this specific date. Simulation results and conclusions drawn from this particular testings impact the final testing of the model's performance.

4.2.1 Influence of Input Magnetograms

To gain insight on the impact the magnetogram has onto the modelling results, a comparison of a result sample using the test simulation for 19-Jun-2011 with 3 different magnetogram inputs (GONG, MWO, HMI) is shown in Figure 4.1. Here the effects of using different input data to the coronal model are depicted. The resolution is 0.5 degrees per pixel. The darkest and brightest colors both represent open fields but of opposing magnetic field. The blue tones lying in between the extremes mark closed fields. One can see that while the maps agree with each other in terms of large scale open areas, overall the appearance is quite different. Using the GONG magnetogram (in the top panel) the structures look most compact with the least small scale variations. This gradually changes from top to bottom, for the MWO and especially for the HMI magnetogram. The topology fragments more in those maps resulting in more small scale elements. This in some regions leads to the breaking up of connected regions, e.g., as at roughly 300 degrees longitude. While structures seem to be connected in the GONG results, this connection is broken when using the other magnetograms as input. A similar thing happens in the HMI result at about 100 degrees longitude. Interestingly, in the GONG results the open region between 20 and 40 degrees latitude is almost non-existent.

Grave disagreement is found in polar regions where the results using the GONG magnetogram produce unipolar open fields, the fragmentation of the other magnetograms also touches onto those regions. This results in an increased amount of closed field structures and even varying polarity at very high latitudes. These occurrences most likely originate from worse line-of-sight visibility at those regions, which leads to a worse resolution (see Section 3.4). Therefore all of the following analysis is mostly restricted to ± 60 degrees in latitude to avoid dealing with these areas of large uncertainties. While the inclusion of flux transport models may partly resolve this issue, ADAPT magnetograms were not available for the two main dates

we investigated.

Note that while in Figure 4.1 the result of only one parameter set $[R_{\mathrm{ss}}, R_{\mathrm{scs}}]$ is shown, other model configurations produce qualitative similar differences when applying different magnetograms. Of course the open areas themselves are also heavily influenced by the parameter set itself, as has been shown already in Figure 4.7 and 4.8 in Section 4.4.2.

4.2.2 Low Resolution Testing and Behavior of Model Parameters

In the test runs it was also investigated how to quickly test if a simulation date is appropriate for the analysis. Furthermore, it was of interest to find out how the model output depends on the parameter configuration in use. For the first question multiple resolutions for the same date (being 13-Nov-2012 - another eclipse date) and just one singular parameter configuration were simulated. The chosen resolution values were $[0.5, 0.8, 1.0, 1.5, 2.0, 2.5, 3.0]$ deg/pixel, where the first one is our default setting. Then, computation time versus output was compared. The resulting computation time was already depicted in Section 3.7 in Figure 3.2. It can be seen that the computation time rises quickly with increasing resolution. We settled on using 1 deg/pixel as the test value, where the simulation run took 1 hour and 42 minutes. In Figure 4.2 it can be seen that with using 1 deg/pixel it is possible to get an appropriate grasp of the detailed magnetic field topology, which is already comparable to the full resolution. With decreasing resolutions (especially with 3.0 deg/pixel as shown in the bottom panel of Figure 4.2) one starts to lose the shape or get misleading sizes of certain structures (see dark regions at slightly above 210 degrees in Stonyhurst longitude). The test shows that the resolution has strong effects on the results and thus has to be carefully chosen.

It has also been of interest to see the influence of the individual parameters on the final outcome. As a showcase of the parameter behavior three configurations are plotted in Figure 4.3 for 11-Jul-2010. From top panel to middle panel, only the source surface parameter has been increased. While most structures retain their general appearance, open structures get smaller. From middle to bottom panel only the Schatten current sheet height is increased. Especially the northern polar coronal hole (in light blue) shrinks drastically in size. It is also expected that R_{scs} has a significant influence on the topology, as this height ultimately cuts all the field lines that are not closed yet and forces them to stay open. Increasing this height naturally results in less open flux. Interestingly this also applies for constant R_{scs} when the

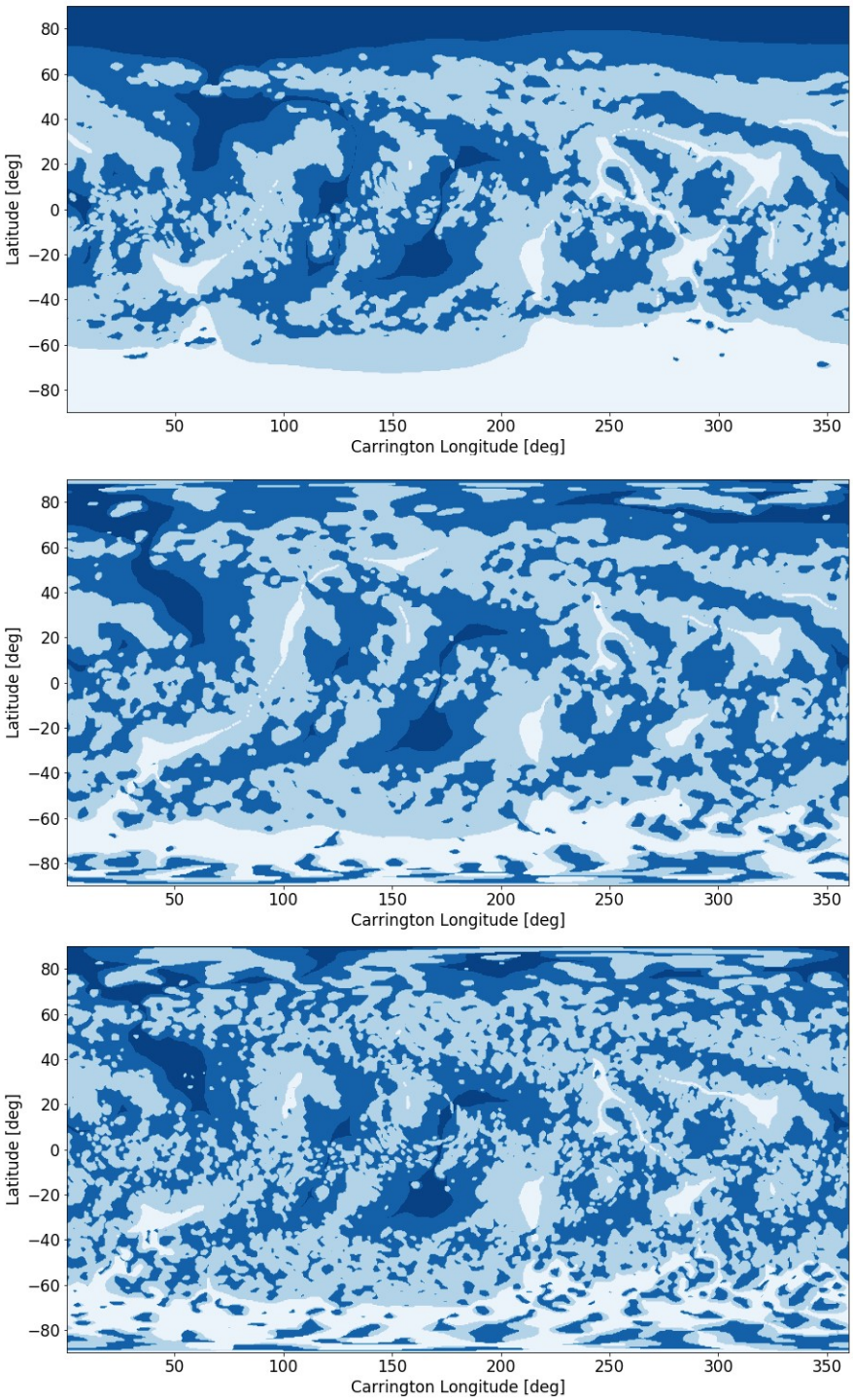

Fig. 4.1.: Influence of the input magnetogram on the modelled topology for 19-Jun-2011. The used magnetograms are from top to bottom: GONG, MWO, HMI, all for the same parameter configuration of $R_{\mathrm{scs}} = 1.4\mathrm{R}_{\odot}$ and $R_{\mathrm{ss}} = 2.1\mathrm{R}_{\odot}$.

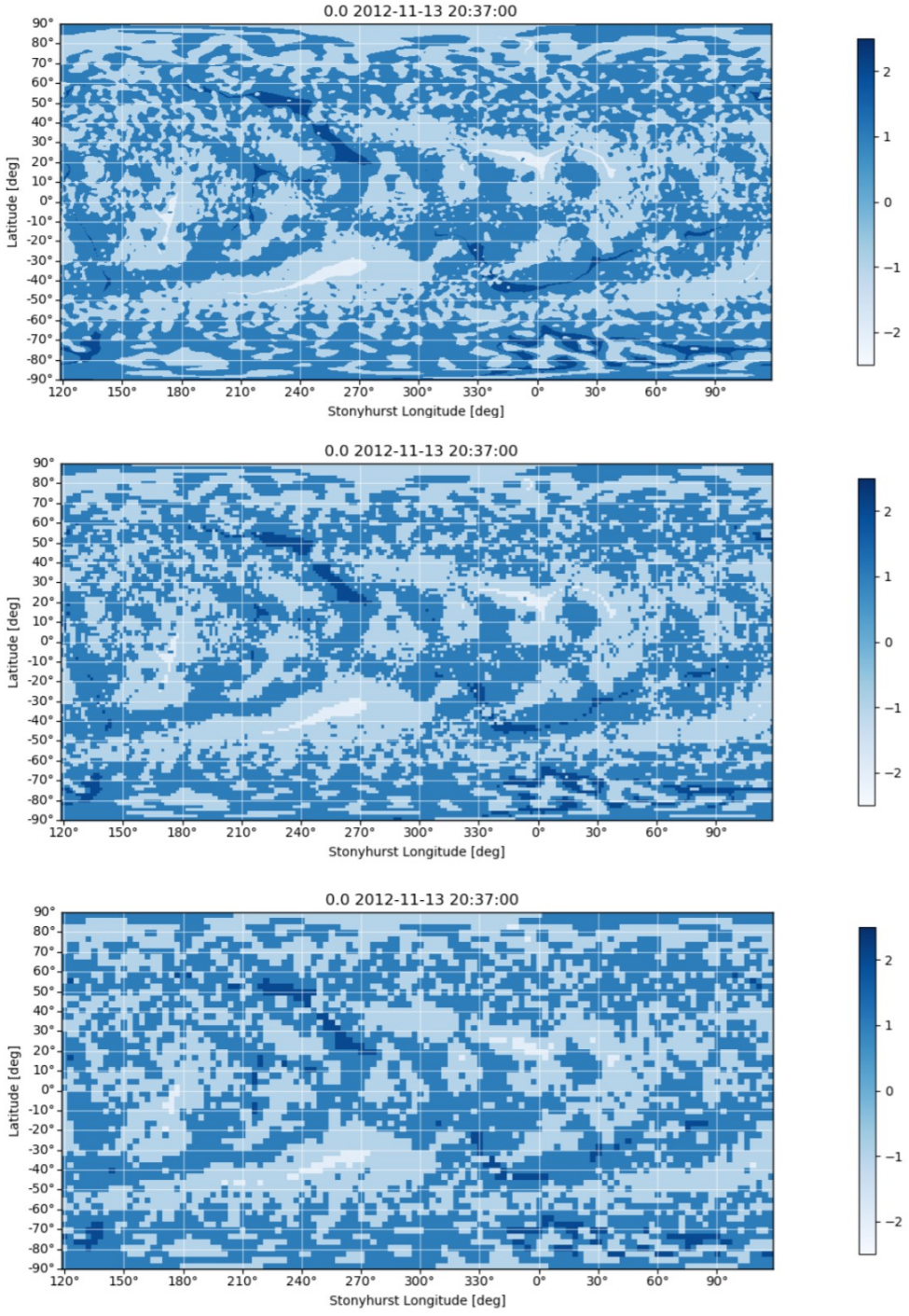

Fig. 4.2.: Influence of the resolution of the input magnetogram on the modelled topology. The used HMI magnetograms are smoothed to: 0.5 deg/pixel (top), 1.5 deg/pixel (middle) and 3.0 deg/pixel (bottom). The used parameter configuration is $R_{\mathrm{scs}} = 1.7\mathrm{R}_{\odot}$ and $R_{\mathrm{ss}} = 3.0\mathrm{R}_{\odot}$ and the simulated date is 13-Nov-2012.

source surface height increases. Without the cut-off via R_{scs} this result would be expected (see Figure 2.1 in Section 2.1), but observing the same behavior with this cut-off parameter is a non-trivial result.

4.3 Additional Experiments

As part of the testing of the model's capacity and different visualization schemes, small experimental results are a natural outcome. While they haven't been investigated in full detail, a short showcase for the sake of completion is given in this Section.

4.3.1 Current Sheet Visualization

Although the PFSS model does not include electric currents per definition (see Section 2.1) the location of the heliospheric current sheet can be estimated. Since this sheet separates regions of opposite polarity (see Section 1.4), an iso-surface at a magnetic field flux density of $B = 0$ can be given as an approximation of this current sheet. A visualization of this is shown in Figure 4.4. Here, a source surface height of $R_{\text{ss}} = 3.0\text{R}_{\odot}$ was chosen - mainly for the reason to have a large modelling domain for the sake of the showcase. Note that this iso-surface not only shows the current sheet but also creates bubble-like structures on the surfaces separating regions of opposite polarity in the vicinity of active regions. One can implicitly see the activity phase of the Sun at the simulation time. While the current sheet in a) has a rather calm structure, while in b) a more complex structure is shown. Indeed, November 2012 is closer to the solar maximum than June 2011 as the solar maximum for cycle number 24 was in April 2014 (Hathaway, 2015).

4.3.2 Synthetic White-Light Images

Another idea for imaging results was the creation of a synthetic white-light image solely based on the output of the magnetic field model. As described in Section 1.1 the white-light component of the corona comes from the scattering of light off free electrons. While the magnetic field and the particle density in the corona are not decoupled, the B-field information alone usually is not sufficient to reproduce the appearance of a coronal image. Unfortunately the PFSS model is only capable of calculating magnetic fields and delivers no information on the density distribution. Therefore an estimation for the coronal density has to be implemented. The presented image in Figure 4.5 vaguely represents an eclipse image applying an inverse r^2 proportionality of the density with height which determines the thickness of the

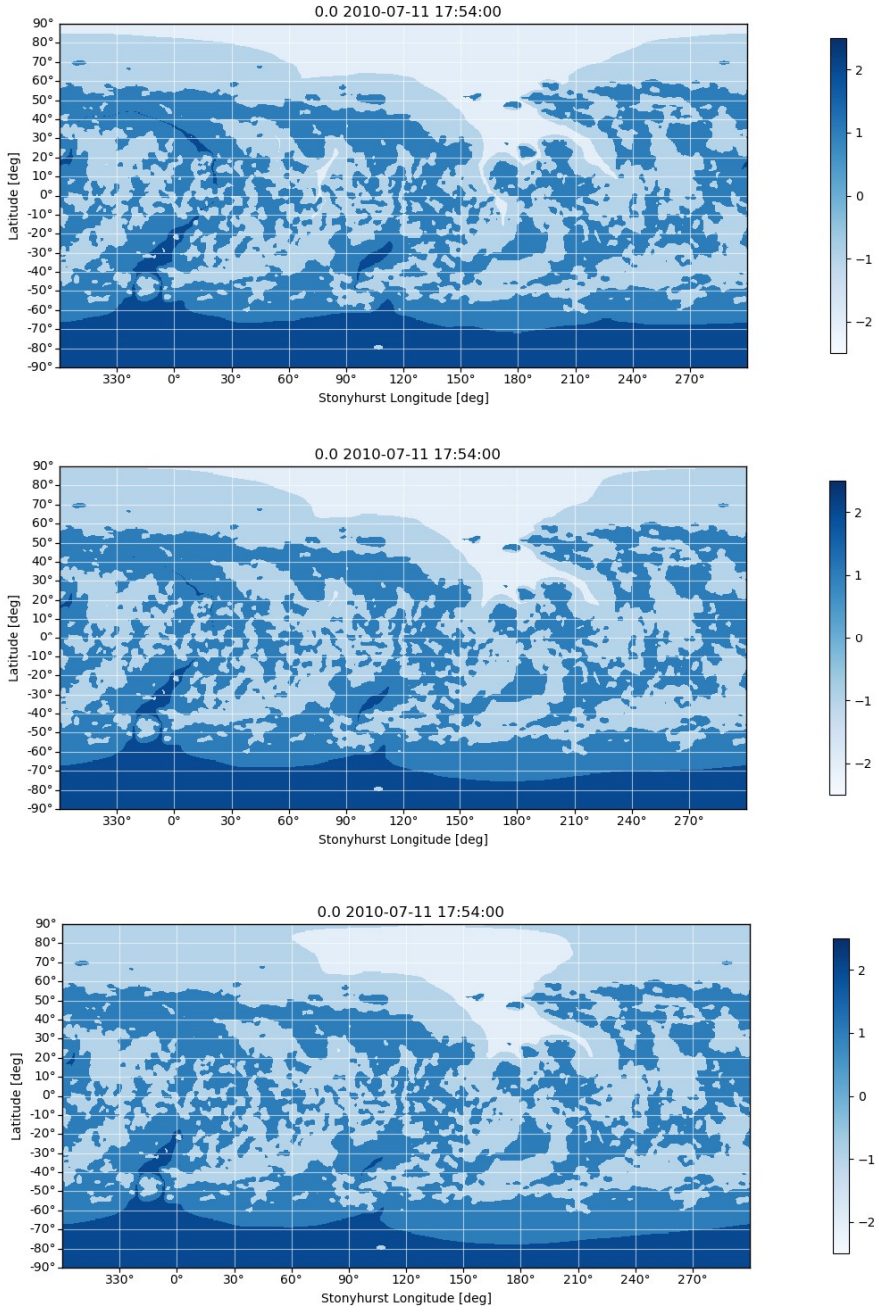

Fig. 4.3.: Influence of the used parameter set on the resulting topology map for 11-Jul-2010 using a GONG magnetogram as input. Top: $R_{\mathrm{scs}} = 1.9\mathrm{R}_{\odot}$ and $R_{\mathrm{ss}} = 2.0\mathrm{R}_{\odot}$, middle: $R_{\mathrm{scs}} = 1.9\mathrm{R}_{\odot}$ and $R_{\mathrm{ss}} = 3.2\mathrm{R}_{\odot}$ and bottom: $R_{\mathrm{scs}} = 2.5\mathrm{R}_{\odot}$ and $R_{\mathrm{ss}} = 3.2\mathrm{R}_{\odot}$.

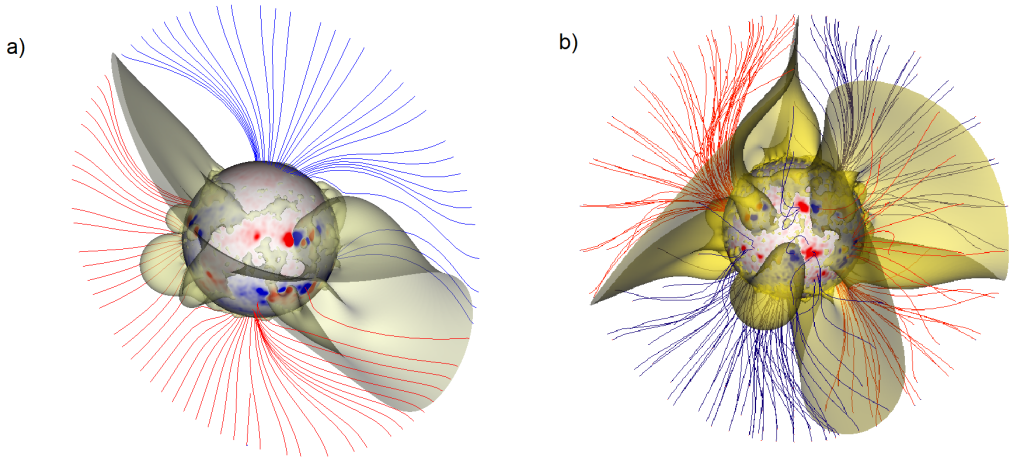

Fig. 4.4.: Current sheet visualization for a) 19-Jun-2011 and b) 13-Nov-2012. The field lines are plotted in a 2D slice using EUHFORIA's PFSS model, where only open field lines have been selected.

field line tubes. The field lines themselves were lit up by the correlation distance parameter from VisIt.

4.3.3 Comparison with PROBA2/SWAP Mosaic Images

While comparisons with white-light images are most intriguing, also EUV images can unveil interesting structures in the solar atmosphere that can be compared to simulated data. For this analysis specially processed data from the SWAP instrument aboard the PROBA2 satellite has been used. Within the solar soft package of IDL a routine is included that combines multiple EUV observations together into one, thus enhancing faint structures that would normally be too weak to be visible in such wavelengths. The resulting images from this combination process are called mosaic images. For the simulation of the solar magnetic field configuration on 11-Jul-2010 mosaic images have been created with various settings (to find the ideal one) and features could be compared to our visualizations, as can be seen in Figure 4.6.

4.4 Quality Assessment of Results

To quantify the accuracy of the model results an assessment scheme has been created, which incorporates both empirical/visual quantification as well as mathematical quantification of the modelled output. The classification scheme itself is divided into 3 sub-steps, that make use of the model-generated topology maps as well as field line overplots onto white-light images (see Section 3.6). The first step is dedicated

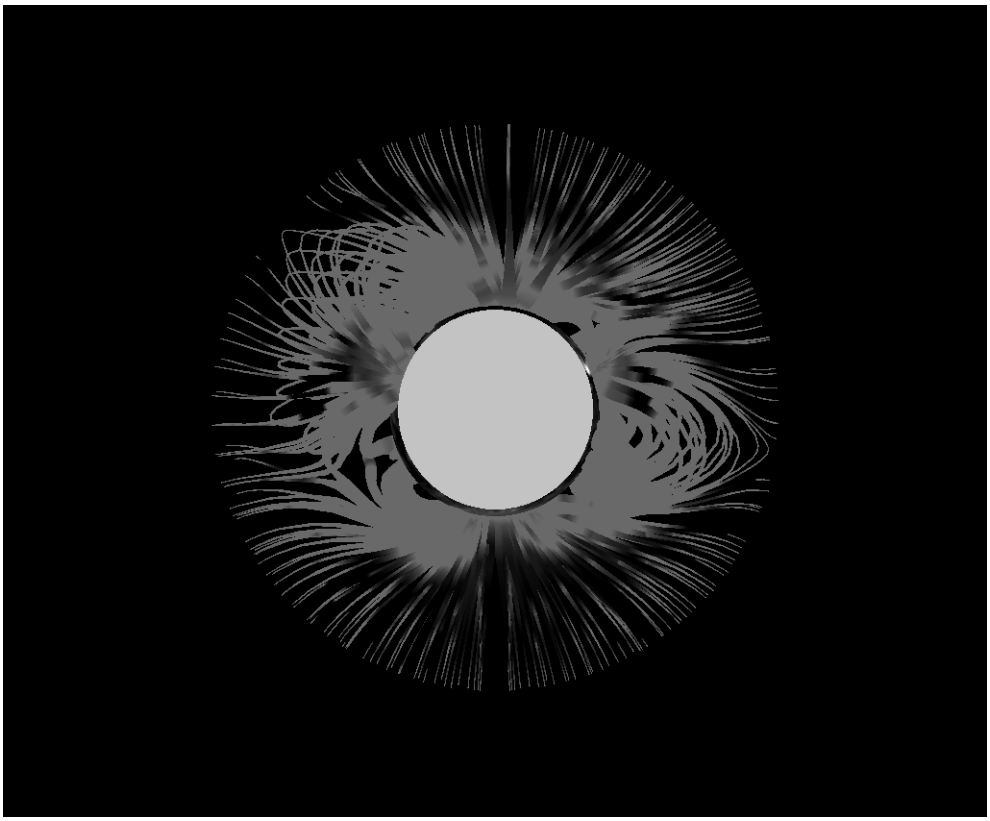

Fig. 4.5.: Synthetic white-light image based on the magnetic field calculation from the PFSS model.

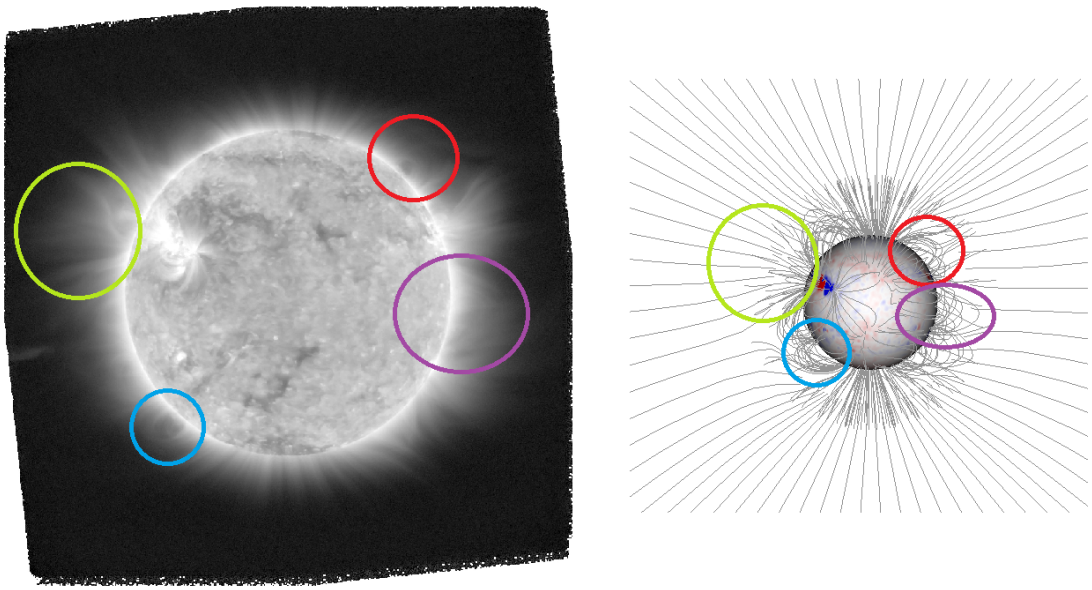

Fig. 4.6.: Identification of features in a PROBA2/SWAP mosaic image (combining data from 17:00 to 20:00 UT) for 11-Jul-2010 with structures in the PFSS field line configuration. Here, $R_{\rm ss} = 1.9{\rm R}_{\odot}$.

to classify the model based on the field lines comparison with white-light data only using empirical measures. In a second step the topology maps, that have already been studied in detail in the previous sections, are analyzed against the EUV Carrington maps of the corresponding Carrington rotation. As a final step the overplots are investigated in greater detail with semi-automatized feature matching methods, implemented in the form of point-and-click algorithms. Putting together the results of all three sub-steps (and the sub-steps within) yields the final classification for the model configurations and the best performing configurations can be evaluated.

For the analysis of EUHFORIA's magnetic field model this developed system was used to quantify the quality of the different parameter sets for the dates 01-Aug-2008 and 11-Jul-2010.

4.4.1 Visual Quantification

Because of the combination of the frozen-in theorem with the low plasma-beta in the lower corona the computed magnetic field lines should approximately match with the plasma density in this region (see Section 1.2). In terms of comparing the computed magnetic field line configurations (especially the PFSS solution) this means that the field lines should match bright regions close to the solar limb. Further away from the Sun's surface streamers are forming as closed, elongated plasma loops (see Section 1.2). The angles at which these streamers extend away from the Sun can be compared with both the location and orientation of the loops (that are in our case given by the PFSS solution) as well as the field line angles themselves (e.g., as originating from the SCS solution).

In the first step the field lines were compared with white-light images in the form of overplots over COR1 and COR2 from both STEREO A and B, LASCO C2 and over eclipse photographs from Druckmüller. This would make six images in total that were classified by eye into two categories: "match" and "no-match". However, the structures that are shown in COR2 of STEREO B are not prominent enough to justify any outcoming results as significant for both dates of interest. Therefore, the comparison with this particular instrument and for these particular dates has been dropped. The criteria for assigning one of the two categories in general has a broad spectrum to choose from and has the potential to be quite subjective. In our case, since a lot of the following methods focus on the PFSS part or the overall topology, we use this step to mostly classify the SCS-introduced bending of field lines close to the domain boundary between PFSS and SCS model. For the STEREO A and B COR1 overplots though the PFSS solution is the only one entirely in range of the visibility of coronal features. Thus, for these two instruments only the PFSS field lines are

compared with white-light features. In this case, the criteria focus on the location of the PFSS-loops compared to the streamer location in COR1.

4.4.2 Open versus Closed Flux

In the following step the open and closed flux will be investigated. The true amount of open flux is here assumed to be emerging from coronal holes, whose areal extension is extracted from observational data with a simple thresholding method. Here, the synoptic EUV Carrington maps (from SOHO/EIT 195 Å and SDO/AIA 193 Å by Hess Webber et al. (2014), and Karna et al. (2014), see Section 3.5) served as comparison material. A binary mask for the field topology is then created which separates open from closed regions. This is done via thresholding based on fixed intensities, which were valued 2.95 for 01-Aug-2008 and 3.5 for 11-Jul-2010 after the logarithm of the maps has been taken. A similar plot is generated from the model output, marking regions of open and closed fields at the source surface on a Carrington map. These two masks are then scaled accordingly to have the same size and coordinates, so pixelwise comparison is possible. Because the mask from EUHFORIA is the smaller one, the EUV map is scaled to the size of the former. A showcase for the results of both dates is given in Figures 4.7 and 4.8. One can see that the outlines of open fields from the EUV are much more fragmented for the EIT map than for the AIA EUV image. Also within the parameter spectrum that we investigated, significant differences of modelled open areas are present. This again highlights the importance of finding and using a solid parameter set, as results are far from stable with varying input (Linker et al., 2021).

To assess the quality of match between the model output and the derived topology from the EUV maps, three different metrics are calculated. These parameters have different implications on the quality of the computed magnetic field structures. They are given in the following:

$$P_{\mathrm{cov}} = \frac{N_{\mathrm{o,b}}}{N_{\mathrm{o,EUV}}} \times 100\%$$

$$P_{\mathrm{Jac}} = \frac{N_{\mathrm{o,b}}}{N_{\mathrm{o,all}}} \times 100\%$$

$$P_{\mathrm{glob}} = \frac{N_{\mathrm{match}}}{N_{\mathrm{tot}}} \times 100\%$$

.

P_{cov} is the so-called coverage parameter, which was already defined in a previous study by Asvestari et al. (2019). It is the ratio of the open pixels in both maps (model

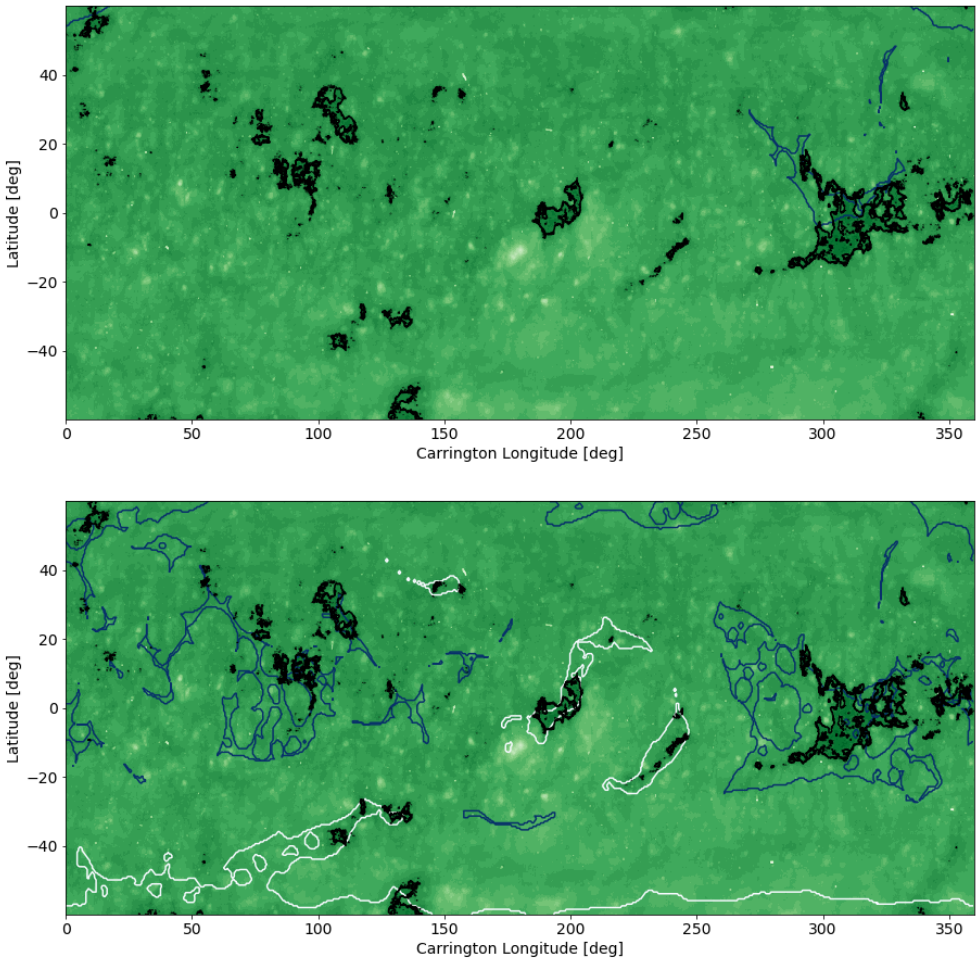

Fig. 4.7.: EIT EUV Carrington map for 01-Aug-2008 with the open areas thresholding outlined in black. Modelled open fields are within the blue (negative polarity) and white (positive polarity) contours. The top panel shows the highest configurations parameter for the model with $R_{\mathrm{scs}} = 2.8\mathrm{R}_{\odot}$ and $R_{\mathrm{ss}} = 3.2\mathrm{R}_{\odot}$, while the bottom one shows the lowest with $R_{\mathrm{scs}} = 1.3\mathrm{R}_{\odot}$ and $R_{\mathrm{ss}} = 1.4\mathrm{R}_{\odot}$.

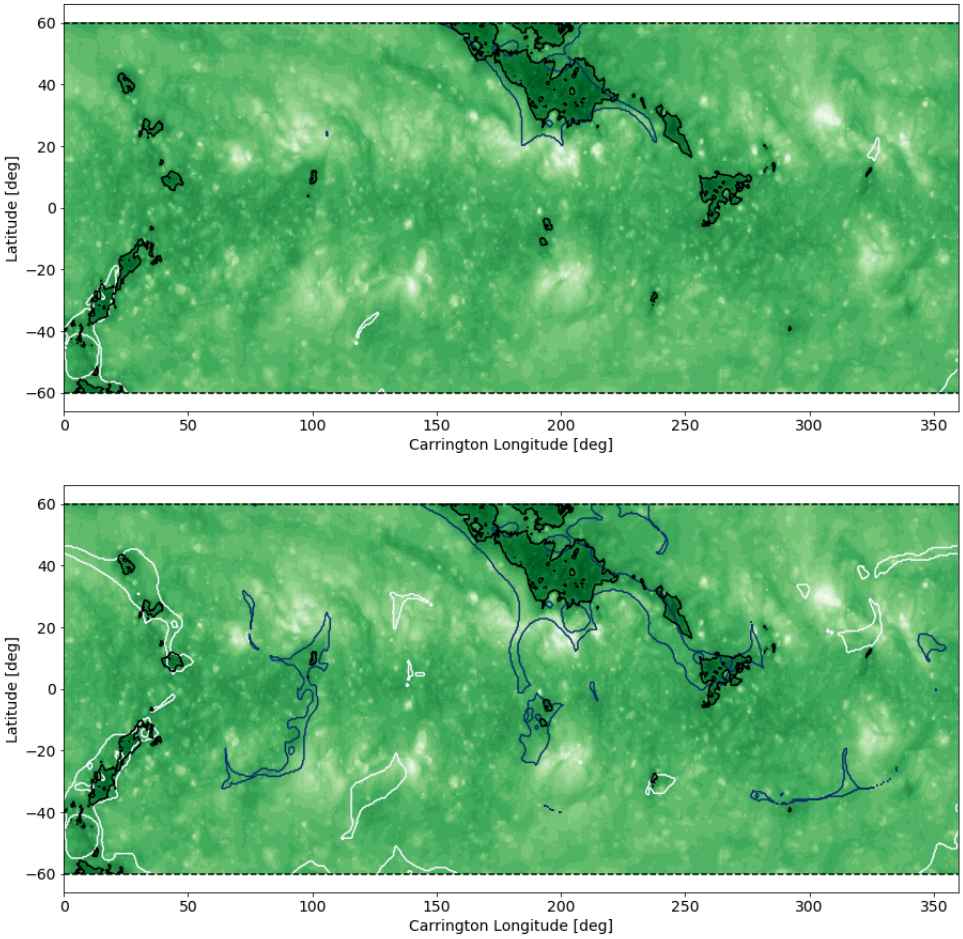

Fig. 4.8.: AIA EUV Carrington map for 11-Jul-2010 with the open areas thresholding outlined in black. Modelled open fields are within the blue (negative polarity) and white (positive polarity) contours. The top panel shows the highest configurations parameter for the model with $R_{\mathrm{scs}} = 2.8\mathrm{R}_{\odot}$ and $R_{\mathrm{ss}} = 3.2\mathrm{R}_{\odot}$, while the bottom one shows the lowest with $R_{\mathrm{scs}} = 1.3\mathrm{R}_{\odot}$ and $R_{\mathrm{ss}} = 1.4\mathrm{R}_{\odot}$.

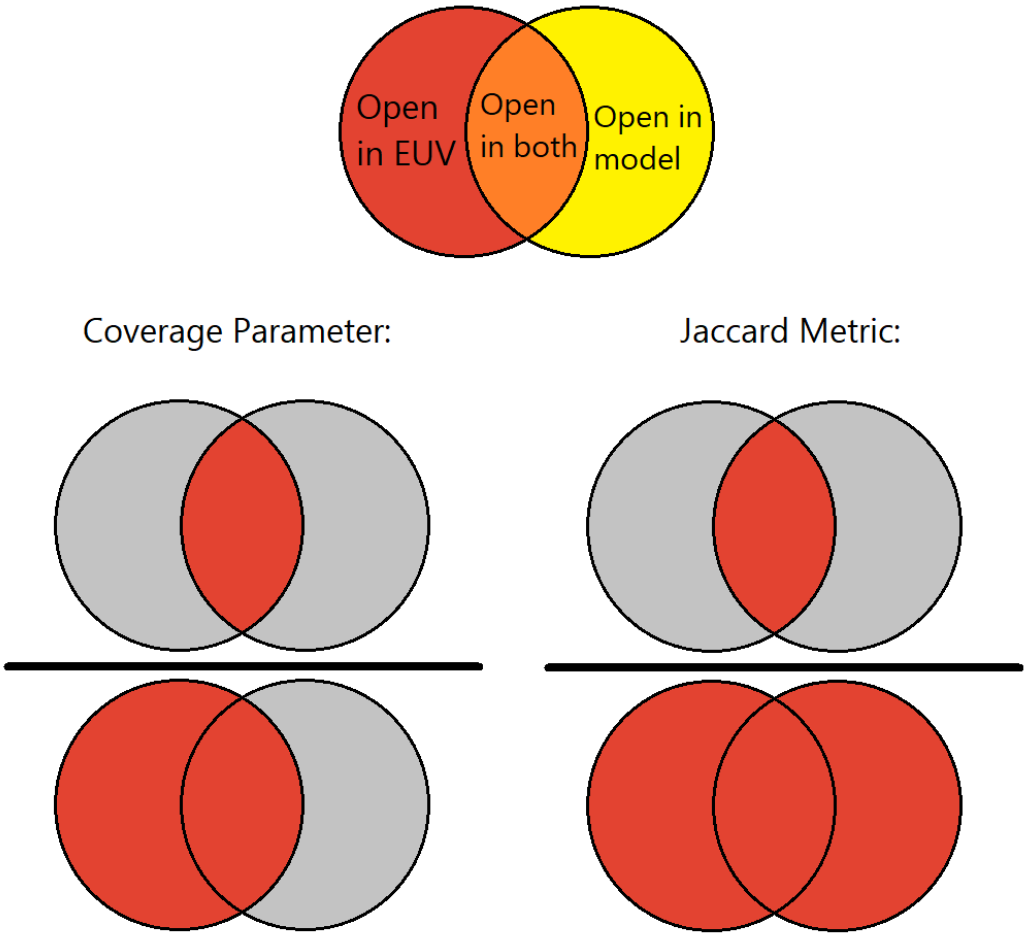

Fig. 4.9.: Visualization of the difference between coverage parameter and Jaccard metric.

and EUV) and the open pixels of the EUV image, thus giving the percentage of overlap of the model open fields with the EUV open fields. Additionally the Jaccard metric P_{Jac} is calculated as the ratio of the open pixels in both topology maps and the sum of all open pixels in both EUV and the model. In contrast to the coverage parameter P_{Jac} also covers the case of the model overestimating the flux, as the models flux is part of the normalization as well. The difference of the two parameters can be depicted with the use of Venn diagrams, see Figure 4.9. The most general parameter one can introduce is the global matching percentage P_{glob}, which is given by the fraction of matching pixels in the masks over the total number of pixels of a map. It is thus not sensitive to the amount of open or closed regions and instead pictures a strict pixelwise comparison of the topology. As all three parameters have fundamental different definitions they don't necessarily need to follow the same trends, as can be seen later in Section 4.5.2. While all three metrics are calculated and analyzed, for the classification system we agreed to use the global parameter P_{glob}, as it reflects best the overall quality of the modelled output.

4.4.3 Feature Matching

For the final method of the classification scheme a more in depth look at the field lines on white-light overplots is taken, as opposed to the rather rough first step of the analysis. It is based on the identification of structures in the model's field line configuration with features in the white-light data. For our analysis of EUHFORIA's coronal model three simple methods have been developed, that investigate a) the difference between the direction of streamers and the direction field lines of the SCS model in close proximity, b) the width of streamers from observational data compared to the width given from the underlying loop structure of the PFSS model and c) the location of the highest loops in white-light versus the location of the highest loops in the PFSS model.

While many different methods and implementations of all levels of complexity can be thought of, it has to be noted that with already very simple point-and-click algorithms adequate results can be achieved. For this reason we opted for this kind of implementation of the above described comparison methods.

Method A: Streamer Angles

For the first method of our feature matching routines, suitable structures in the white-light images had to be chosen. Besides choosing prominent features, also the brightness is crucial as our analysis is based on the assumption that the streamers we investigate lie approximately in the plane of sky. We are restricting our analysis only on the features with high intensities. This is then in accordance with the theory of Thomson scattering, that states that the maximum brightness is approximately reached in the plane of sky (see Section 1.1). We thus can compare the SCS field lines that are visualized in a 2D-slice of the plane of sky with the selected streamers (see panel a) in Figure 4.11). For this purpose we are using STEREO/COR2 and SOHO/LASCO C2 data, as these instruments have a suitable field of view for assessing the SCS model's performance. Note that, since there were no streamers bright enough in STEREO B's COR2 for both dates of interest, no analysis of STEREO B COR2 images has been done in this sub-step though.

At two fixed heights we then compared the difference between the streamer angle with the angle of the closest SCS field line. It was decided to fix those two heights at $H_1 = 3.5\mathrm{R}_\odot$ and $H_2 = 6.0\mathrm{R}_\odot$. The values come on the one hand from the restrictions of the field of view by the instruments as upper boundary. On the other, at too low heights model field lines as well as streamers are not following approximately radial trajectories (which would bias any angle derivations). Therefore, this lower boundary was chosen.

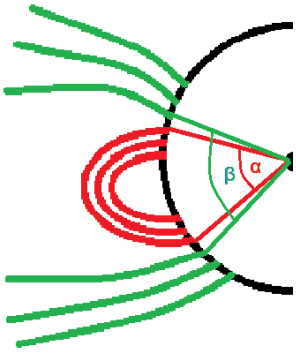

Fig. 4.10.: Illustration of two different streamer width definitions from the underlying magnetic topology of the model. α is the width of the closed structure as defined by the outermost loops, while β is the width defined the nearest open field lines.

Method B: Streamer Width

As a next step, streamer widths are derived again through a point-and-click routine from the observational data of STEREO/COR1 for both dates under investigation. The extracted width is then compared via the same procedure to the extension of underlying closed magnetic structures (i.e., loop systems) in the PFSS model results (see panel b) in Figure 4.11). Since these widths vary with height and deviate from loop systems with increased distance from the Sun, a comparison height of $H = 1.75\mathrm{R}_{\odot}$ was chosen. At this height outflowing streams and loops are still coupled together (if one sets this radius too high: transition of $\beta < 1$ to $\beta > 1$), while also reaching above the occulter edge of the COR1 coronagraphs, which is obviously a necessary condition for the analysis. Naturally configurations where R_{ss} is below H are excluded from the analysis as no loop systems reach there. It has to be noted though that also configurations with $R_{\mathrm{ss}} > H$ sometimes don't show loops reaching H. The comparison parameter here is the angular difference between the loop extension and the streamer width at height H.

The definition of the extension of the closed regions below streamers is non-trivial in the frame of the field line picture. Since there is no continuous transition from loops to open field lines, the margin in between outer edge of loops that show up in the visualization and the nearest appearing open field lines marks a source for uncertainties (see illustration in Figure 4.10). To quantify this uncertainty the analysis is done with both definitions. The two resulting values are then averaged, where the difference resulting from the two definitions enters into the error calculations.

Method C: Brute Force Matching

As a last implementation we incorporated a simple form of brute force feature matching. Its aim is the comparison between the location where features appear in the white-light data versus where they appear in the model. As a reference point which is present in both the model and observational images, the apex loop structures are chosen (see panel c) in Figure 4.11). This unfortunately proves to be difficult to analyse for coronagraph data. Here the strength of choosing an eclipse date comes into play: In high resolution solar eclipse images loop systems can be viewed in great detail and enables properly carrying out this kind of comparison.

The classification parameter is then the difference between the locations of the loop apex of the highest loops of a certain structure in the model and the estimated loop apex of the highest loops in the observations. The distance between the two points is converted to units of solar radii.

4.5 Application of Benchmarking System on 01-Aug-2008 and 11-Jul-2010

With the gained insights from Section 4.2.1 we opted for using a GONG magnetogram for 01-Aug-2008 (as no HMI is available for this time) and an HMI magnetogram for 11-Jul-2010. The coronal model is set-up using all of our 67 parameter configurations with a resolution of 0.5 degrees per pixel and using solid harmonics up to the order of 140 for the PFSS calculation (cf. default value in Section 2.5.1). With these settings we compared our simulation with observational data as described in detail in Section 4.4 and the results are presented in the following.

4.5.1 Visual Inspection Results

As a first step we inspected the field line overplots, where field lines originating from the model results are plotted on top of white-light images. We then investigated the SCS field line bending comparing to streamers in LASCO/C2, STEREO A/COR2 and Druckmüller's high resolution eclipse images. As already discussed in Section 4.4.1, the reason for the exclusion of STEREO B/COR2 data for both dates the image data did not reveal significantly bright features with sufficient radial extensions. Thus, the assumption of comparing our 2D plane of sky slice SCS results to structures that lie approximately in the same plane breaks down. For visually assessing the PFSS model's 3D results we used both STEREO A/COR1 and STEREO B/COR1 data.

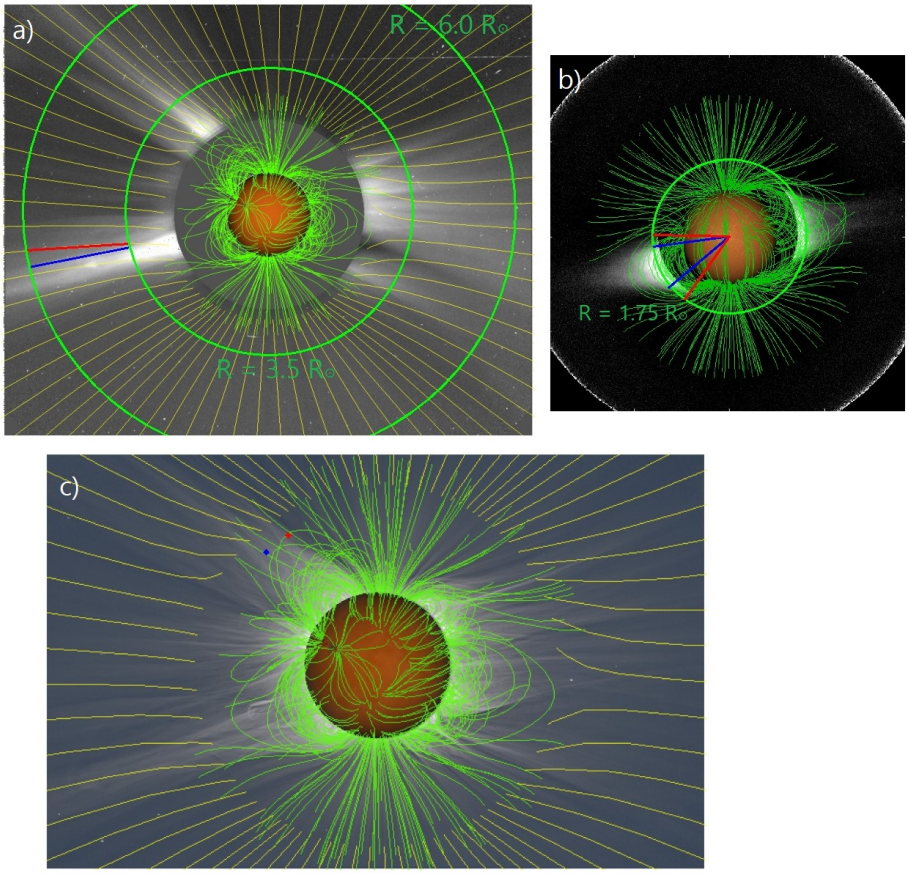

Fig. 4.11.: Visualization of the three feature matching methods with a) the streamer direction comparison, b) the streamer width derivation and c) the brute force feature matching. Blue lines or marks are results from the observational data, while derivations from the model are colored in red. Green field lines mark the 3D PFSS solution while yellow field lines depict the 2D SCS result.

From our analysis the ideal SCS parameter lies within $R_{\mathrm{scs}} \in [1.5, 2.1]\mathrm{R}_{\odot}$ for both while the results for the source height seem to deviate more from each other, but generally favoring configurations in the mid-field of the used parameter spectrum.

4.5.2 Topology Classification Results

In the next step following our benchmarking system we investigated the model's topology output and compared it to the SOHO/EIT and SDO/AIA Carrington EUV maps as described in Section 4.4.2. The results for the different comparison metrics are shown in Figure 4.7 and 4.8. As explained in Section 3.4 the analysis is restricted to ± 60 degrees in latitude to avoid problems coming from projection effects.

For 01-Aug-2008 we see that all three parameters behave differently. While there comes a turning point when increasing R_{scs} and R_{ss} in P_{Jac}. The peak itself is quite low with only roughly 14%. P_{cov} shows a continuous decrease with increasing the configuration parameters, while P_{glob} behaves inversely. While for 11-Jul-2010 the coverage parameter still follows the same trend, as expected from the discussion above, P_{Jac} now on the other hand seems to behave similarly to P_{glob}, which follows the same trend for both dates. It is favoring higher parameter values and thus less open field from the model for this date.

Comparison between the results from 2010 and 2008 yields that the 2008 results for the metrics (except P_{glob}) are numerically significantly lower, which means that the model's results fit the topology of the EUV notably worse, when focusing on the open fields only. For P_{glob} the results are very similar in peak values, where for both dates the best configurations peak at roughly 96%, but the spread in values for 01-Aug-2008 is bigger. Thus, the worst configurations reach lower in P_{glob} at under 86%, compared to over 88% for 11-Jul-2010.

4.5.3 Feature Matching Results

In the following the results of the feature matching methods, described in Section 4.4.3, are presented. All of the comparisons are carried out as already mentioned via point-and-click routines, since their implementation as well as application is rather simple, but effective.

Method A: Streamer Angles

The results of the first sub-step are shown in Figures 4.14 and 4.15 for 01-Aug-2008 and 11-Jul-2010, respectively. As it was the case in the visual comparison in Section

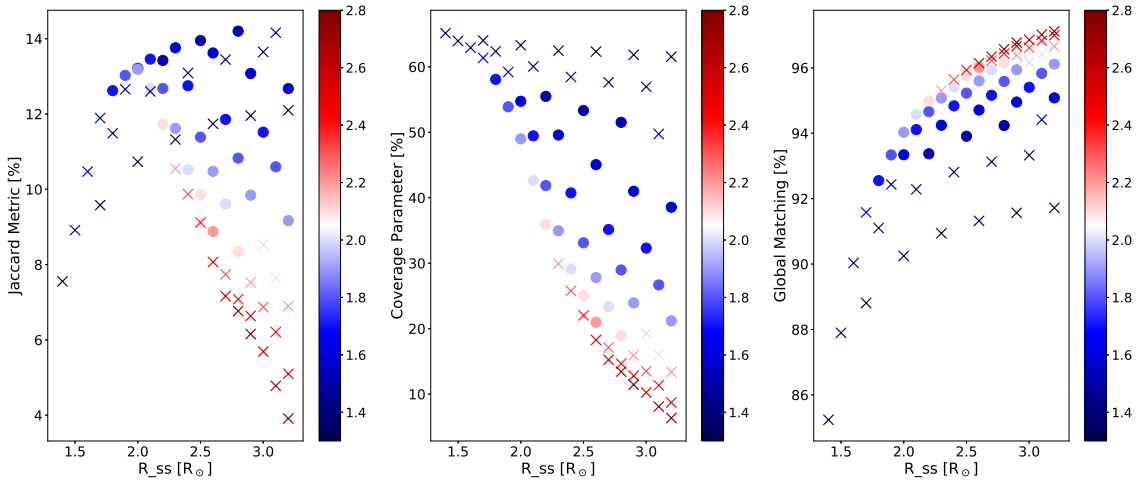

Fig. 4.12.: Results for different topology metrics for varying PFSS and SCS heights for 01-Aug-2008. With the colorbar the value of R_{scs} in units of $\mathrm{R}_{\odot}$ are indicated, while circles mark configurations that passed the visual inspection and crosses mark configurations that did not pass.

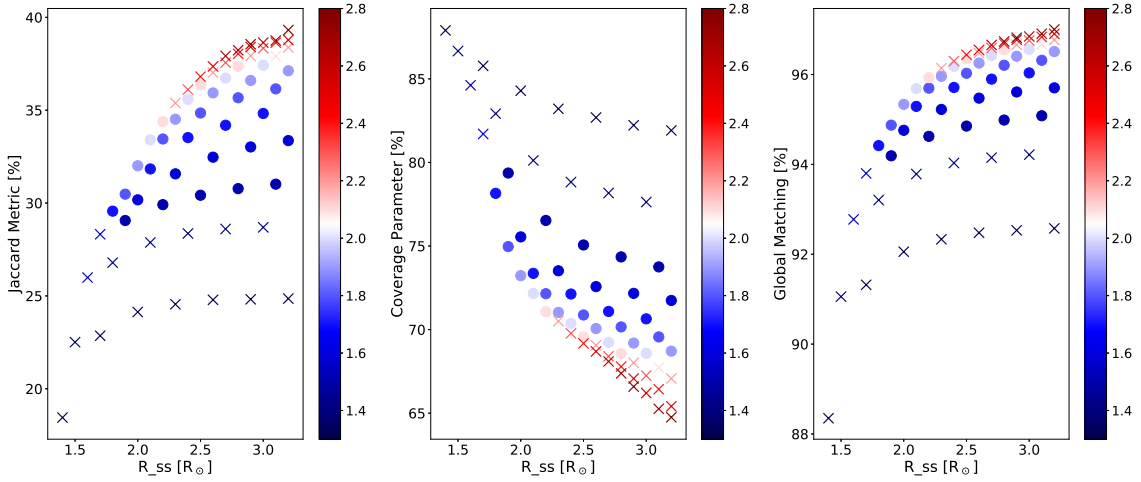

Fig. 4.13.: Results for different topology metrics for varying PFSS and SCS heights for 11-Jul-2010. With the colorbar the value of R_{scs} in units of $\mathrm{R}_{\odot}$ are indicated, while circles mark configurations that passed the visual inspection and crosses mark configurations that did not pass.

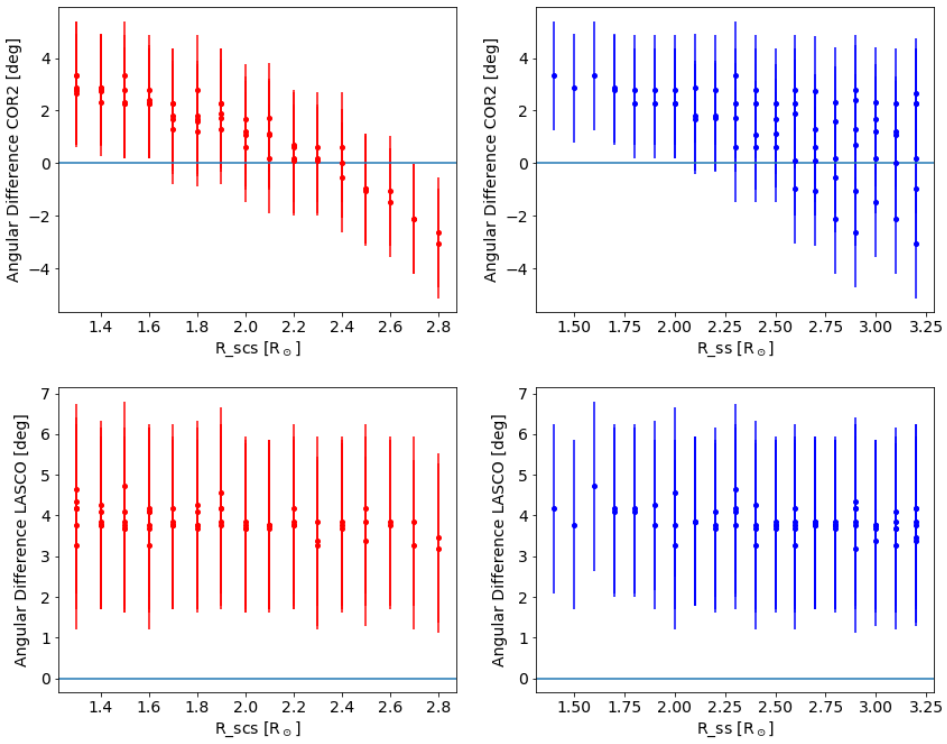

Fig. 4.14.: Angular differences between modelled streamer angles from the SCS model and streamer angle as derived from observational data between the heights of $H_1 = 3.5R_\odot$ and $H_2 = 6.0R_\odot$ for 01-Aug-2008.

4.5.1 no STEREO B/COR2 data has been used because of the lack of sufficiently bright streamers. Therefore referencing to COR2 always means the instrument aboard STEREO A. For 01-Aug-2008 one feature per coronagraph image was analysed, for 11-Jul-2010 an additional feature in the COR2 image was compared. Apart from the feature in LASCO C2 of the 2008 eclipse date (where no conclusions to favor a specific configuration can be drawn from), a variation in the field line angle with rising SCS height can be observed. Note that rising and declining slopes are just unveiling the direction from which the field lines approach the derived "true" streamer angle. Multiple dots for the same SCS height imply the different PFSS heights and vice versa. This shows that the results are mostly dependent on R_{scs} as there is no significant spread in the graphs for the same value in R_{scs}.

The errors are derived by tilting the SCS visualization slice by ± 10 degrees in longitude. Then the standard deviation is given by the mean variation of the field line angles. This estimates the uncertainties for the case that the chosen streamers are not exactly in the plane of sky, but within ± 10 degrees of the visualized 2D SCS-slice.

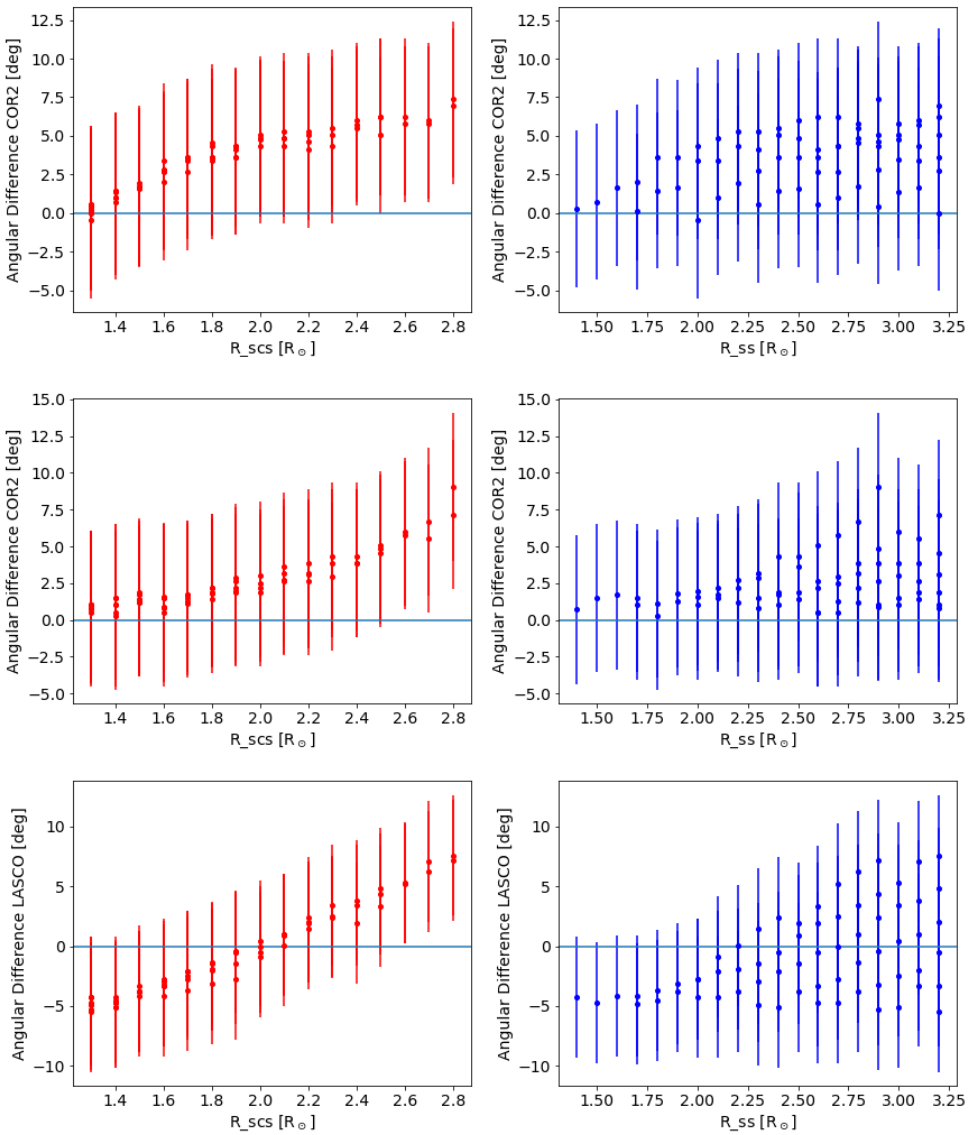

Fig. 4.15.: Angular differences between modelled streamer angles from the SCS model and streamer angle as derived from observational data between the heights of $H_1 = 3.5R_\odot$ and $H_2 = 6.0R_\odot$ for 11-Jul-2010.

Method B: Streamer Width

For the second step of the feature matching implementations the streamer widths were investigated. The corresponding results of this analysis are shown in Figure 4.16. One can see that similarly to the SCS analysis in the prior step, the configurations with the highest parameter values deviate the most from the derived observational streamer widths. Also the results between the two dates agree quite well with each other. The only significant difference is that while in the 01-Aug-2008 STEREO A data the lowest R_{ss} produce bigger angular differences, for 11-Jul-2010 the STEREO A data follows the trends of both STEREO B data where the lowest R_{ss} deviate more from the observationally derived values. The best agreement with the COR1 data is found in the lower middle range of the parameter spectrum around 2.4 $\mathrm{R}_{\odot}$ for R_{ss}. While source surface heights below 2.0 $\mathrm{R}_{\odot}$ could not be investigated due to those configurations not producing loop systems reaching the necessary height (most not even surpassing the occulter edge) no analysis for them could be done. If one follows the presented trends though one can make an educated guess that these configurations would not produce the best results anyway though.

The errors are calculated by the previously discussed angular difference between the width as derived from the outer loops of the system and the nearest open field lines and by the visualization bias. This uncertainty originates from the visualization method - as we have to "choose" a certain set of field lines to plot, we introduce a natural bias. To derive this error, multiple sets of different field lines are visualized with which the analysis is done. Again, the variation that is introduced through the various sets of field lines defines the standard deviation.

Method C: Brute Force Feature Matching

For the last step a direct comparison between features in observations and the models is carried out. In particular, the location of prominent structures is compared to the location of the corresponding loop system. Because, as pointed out in Section 4.4.3, the loop apexes are used for comparison. Because of the difficult identification of the apex locations in coronagraph images, only the eclipse images are used.

The results of this analysis are shown in Figure 4.17 for two features in the image from 01-Aug-2008 together with one feature from 11-Jul-2010. It can be seen that trends agree very well within the range of computed R_{ss}, where heights in the lower 2.x $\mathrm{R}_{\odot}$ are favored. Only few minor outliers are present that mostly come from the first feature of the 2008 eclipse date. This result is also in general agreement with the outcome from the previous step in Section 4.5.3, where similar heights seem to be fitting best. The errors are originating from the visualization bias, with the calculation being analogue to the error derivation for Method B.

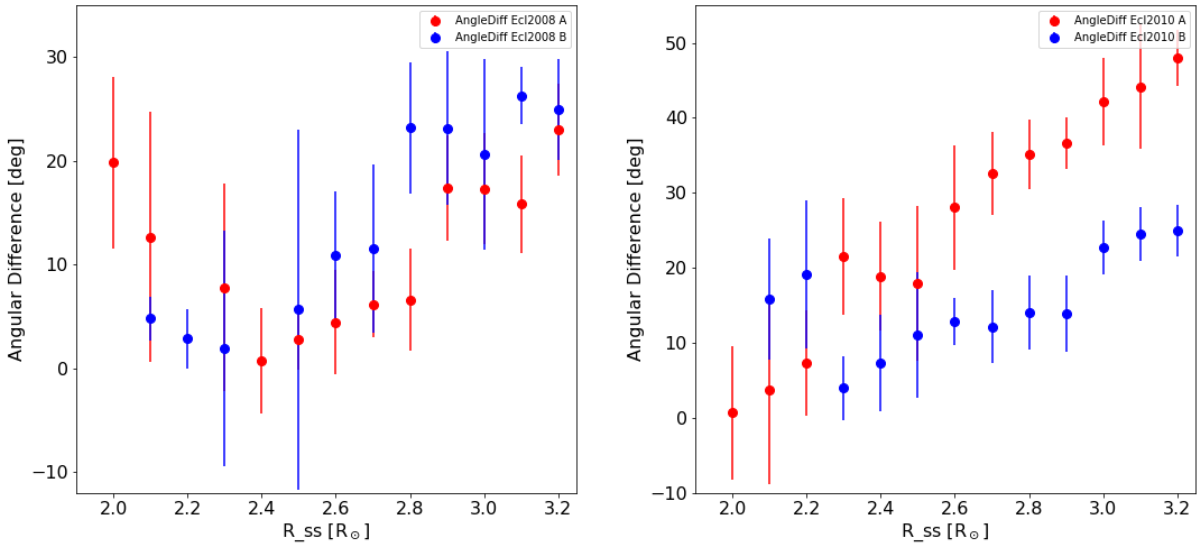

Fig. 4.16.: Difference in angular width of streamers versus width of loop structure at a height of $H = 1.75\mathrm{R}_{\odot}$ for 01-Aug-2008 and 11-Jul-2010.

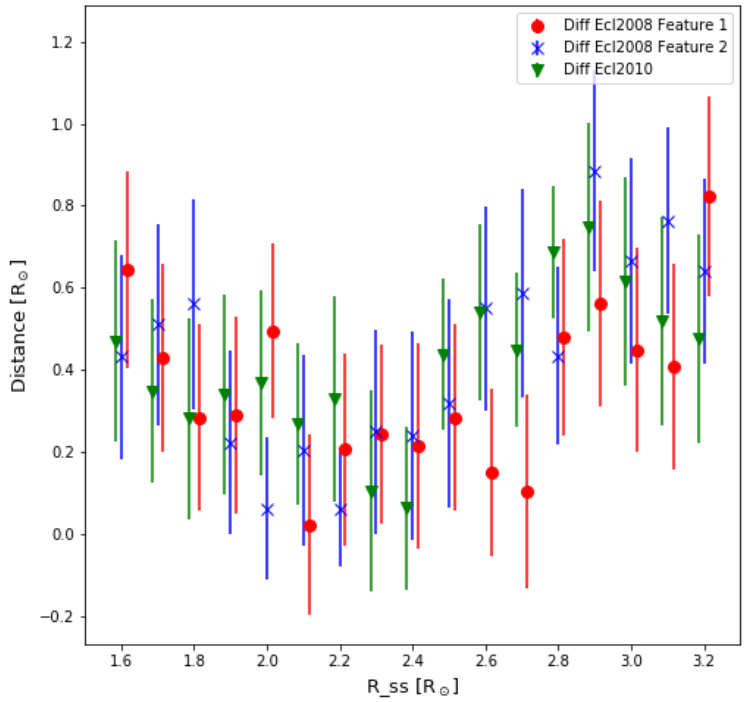

Fig. 4.17.: Brute Force Feature Matching results for both 01-Aug-2008 and 11-Jul-2010 using Druckmüller eclipse images.

4.5.4 Combination of Results - Final Classification

To arrive at a final result after all the analysis steps have been concluded, a system for merging all singular outcomes into a final class has been made. This scheme is pictured in Figure 4.18, which is applied for both dates of interest. If the analysis method is only investigating the PFSS model, the set size of analyzed parameters R_{ss} is 19, while if the SCS model is included all 67 parameter configurations are analyzed.

All parameter configurations whose field line visualization matches well in at least 3 out of the 5 comparative images (i.e., the field line overplots on white-light data) get sorted into category A. For the topology comparison with EUV Carrington maps the top 50% of configurations are advanced into the category B, judging by the global matching parameter P_{glob}. In order to categorize the outcomes of the feature matching routines, the results of Section 4.5.3 have to be combined. A field line configuration is marked as "matching" if the derived quantity (e.g., the streamer width) lies within 1σ error range. For the streamer direction comparison configurations, that fulfill this criterion at least for one of the two instruments, is classified as "matching". For the other two sub-steps matches in all used comparative images have to be achieved in order to be classified as "matching". This discrepancy is due to the reason that the field lines for the used feature for LASCO C2 in 2008 showed no variation. Thus, applying the same measures as for the other two feature matching routines would result in the exclusion of every configuration in this case. Finally, if two or all three of the combined results for the feature matching methods showed good quality, then those configurations advance into the category C.

This three sets of parameter configurations are then used to arrive at a final classification for the overall analysis: Parameter sets that are present in two of the sets A, B or C are classified as "Ok Configurations", while configurations that are found in all three sets are classified as "Best Configurations".

For 01-Aug-2008 we have 30 configurations in category A, the obligatory 33 in category B (as the sample is halved per definition in this step) and 11 configurations in category C. Finally, we arrived at 21 configurations that are "Ok", while the number of "best" configurations is only 3. For 11-Jul-2010 on the other hand 32 configurations are found in A, 33 in B and again 11 in C. While there are still 19 configurations classified as "Ok", only 2 configurations are marked as "best configurations". An interesting detail is that there is one configuration that is marked as "best" for both dates, meaning that this configuration succeeded in every main step and is found in all six sets (three for each date). This parameter configuration is $[R_{\mathrm{scs}} = 2.0\mathrm{R}_{\odot}, R_{\mathrm{ss}} = 2.4\mathrm{R}_{\odot}]$.

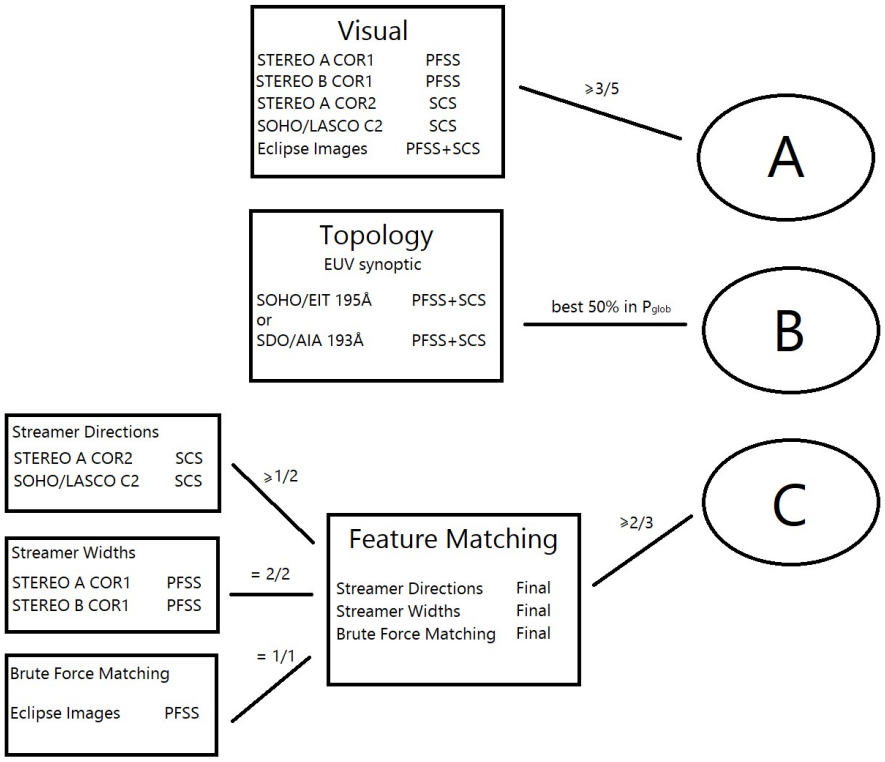

Fig. 4.18.: Classification Scheme for assessing the best model configuration, given the presented analysis steps. On the right-hand side in each box there is the comparative image data, except in the "Feature Matching" box, where on the right side there are the results of each sub-step. Configurations that pass the analysis carried through in each box are sorted into the sets A, B and C.

5 Discussion

In this chapter the results obtained in Section 4.5, i.e., the outcomes from the visual inspection, topology analysis and the feature matching, are interpreted and discussed.

This sub-step is obviously the most subjective one, which can lead to the highest variance in results, depending on the person judging the quality of the parameter configurations. The SCS comparison is straight forward as a fixed criterion was set with the bending of the field lines that has to match the bending of features at streamer locations. As pointed out in Section 4.5.1 the results all seem to agree on a certain parameter range here, while this is not the case in the PFSS comparisons. The reason for the higher discrepancy in ideal R_{ss} could lie in the current state of the Sun at the given times. While in COR1 of STEREO A for 01-Aug-2008 two very large features can be seen, the situation is different for STEREO B COR1, where there are smaller streamers present instead. This results in configurations producing bigger, large-scale loop structures to fit better to STEREO A COR1, while the inverse is true for STEREO B. The same also applies for 11-Jul-2010. This implies that, if investigating the PFSS solution on those two simulation dates only, the model would benefit from a non-spherical, varying source surface, such that bigger features can be matched by the model independently of the fitting of smaller structures. In fact, such PFSS adaptations have already been suggested and used (see e.g., Kruse et al., 2020).

While it is best to use full on-disk solar EUV maps for comparing the magnetic topologies of models and observations, those maps come with natural downfalls. One has to keep in mind that the synoptic nature of the Carrington EUV maps also means that not only data from the date of interest is included, but the data is not static in time, which is needed to construct the full 360 degree map. This has the drawback that dynamic processes happening in the time span that the Carrington map is created may change the open/closed fields as observed in EUV (the same applies for the input magnetograms as well though). One can observe small shifts and deviations in our comparison, when taking a closer look at Figure 4.8. The Carrington rotation that covers this date starts at 16-Jun-2010 and lasts until 13-Jul-2010. There are regions where the general topology of the model fits quite well to the EUV image, while in other regions it seems that there are slight offsets in

longitude of certain features. Despite these discrepancies, the method seems to overall work well as (for testing purposes) applying systematic shifts produce only insignificant differences on the end result.

The difference between the individual metrics originates partially from the different normalizations, but also from the different statements that each parameter presents. Because P_{cov} increases with increased overlap of modelled open areas with EUV open areas, it is a natural consequence that this parameter rises with increasing R_{scs} and R_{ss}, as higher values of those parameters automatically produce more open fields (see discussion in Section 2.1). This can be seen in the results for both dates in Figures 4.7 and 4.8. P_{Jac} on the other hand is also sensitive to overestimation of open flux by the model. For 11-Jul-2010 both P_{Jac} and P_{glob} follow similar trends, preferring configurations that produce less open fields. This leads to the conclusion that the overestimation of open flux from the model is an issue in this case. This is also reflected in the discrepancy between P_{Jac} and P_{cov}: Here more open fields (i.e., lower parameter values) increase the overlap with EUV coronal hole areas (thus P_{cov} increases), but this effect is overcompensated by the overestimation of open fields. Thus, P_{Jac} is behaving inversely to P_{cov}. The overestimation can also be seen when looking at the amount of open pixels in both the EUV mask and the masks from the model results. Even for the configurations with the least open flux, the amount of open pixels is still higher (with 6708 = 3.88 $\%$) than the number of open pixels from the EUV mask (with 5181 = 3.00 $\%$).

For 01-Aug-2008 the situation appears to be quite different. While for the global field topology, still the highest configurations seem to be favored, P_{Jac} follows a significantly different trend than for the 2010 eclipse date. Theoretically systematic offsets could lead to different results though. This has been investigated and systematic shifts of 3 and 5 degrees yielded a minimal change of under 1.5% in the worst cases for P_{Jac} and significantly lower changes for the other parameters.

The global parameter though always is the largest amongst the defined metrics. An explanation can be given by the fact that most of the field is closed and correctly modelled, while accurately modelling the spots of open fields is the difficult task to solve. Thus, the parameters revolving solely on the open topology have lower values. It also has to be noted that while the source surface height indeed has an influence on the modelled field topology, the dominating parameter is R_{scs}. This observation was also made already in Section 4.2.2. The most interesting feature in the results of both 2008 and 2010 is that fact that when marking the outcomes of the visual inspection, both the best and worst configurations of this topology comparison would be cut out in most cases. An exception to this behavior can be seen for 01-Aug-2008 in the Jaccard metric, where most of the highest P_{Jac} values also seem to pass the visual inspection. The general discrepancy though highlights

the strength for having both steps featured in the validation scheme, as each step investigates very different features of the solar magnetic field (which also the model seems to reproduce at varying quality).

As shown in Section 4.5.2 the values for different dates for the same metrics deviate quite significantly (except the global parameter). Reasons for the differences might be coming from the used EUV maps, the thresholding or the different activity phase of the Sun. For the latter though, one would expect the PFSS model to perform better for quiet-Sun phases, which would mean that the 2008 date should in theory fare better than the 2010 date. The inverse is the case though! Using different thresholds for defining open regions in the EUV obviously varies the results of the analysis. This problem is not trivial to deal with when using empirical thresholds (as was done in this analysis). An issue could also be that around the time of the eclipse, a plasma structure is visible that was ejected from the Sun. This kind of activity can not be resolved by the model, as it is not able to model dynamic phenomena. Solar activity can alter the magnetic structure of the solar corona and thus influences the quality of our results. Furthermore, the outlines of open fields are a lot more noisy in the SOHO/EIT than in SDO/AIA map. This could also be a source of the discrepancy. For future implementations it could be useful to stick to the same EUV instrument to avoid such differences. The reason we did not go this route lies in the fact that we wanted to use the best available instrumental data for the dates of interest, which yielded EIT for 2008 and AIA for 2010.

The first of the feature matching methods, the streamer direction analysis, is almost solely dependent on the SCS height as observed in Section 4.5.3. While the ideal parameters for this sub-step are not clearly derivable as the errorbars are quite large, all results seem to agree that high R_{scs} values are producing worse results. This result is also in agreement with the visual classification, which is expected as both substeps make use of the same image material. It has to be noted that some SCS field lines in the visualizations seem to stay stable over all configurations and thus no variation can be derived as was the case for the LASCO perspective for 08-01-2008. The option to use a fainter structure for comparison where the field lines are more unstable would contradict the assumption of the feature under investigation lying approximately in the plane of sky. This result was therefore kept in the analysis for consistency and completion. The errors as derived in Section 4.5.3 via tilting the visualization slice are dominating over the point-and-click accuracy, so it can be neglected.

A more clear derivation of ideal parameters can be made from the following two methods. The streamer width analysis results yield a strong filter as deviations from the observational widths can get quite large (on the order of a few tens of degrees). The discrepancy between the 11-Jul-2010 STEREO A result and the others

could lie in the chosen feature. As higher source heights R_{ss} produce larger loop structures, investigating smaller structures will always lead to a favouring of lower R_{ss}. Indeed, this is the case for the 2010 date in the STEREO A perspective. On the other hand, also the feature of interest for 2008 in STEREO B has a significantly smaller width than the other two, but follows the same trends. Another reason could be that the instrumental data for 2010 does not have this sharp and clear structures, as were present in 2008, due to the activity level of the Sun and/or instrumental degradation. The variable errorbars originate from the variable distances between open boundaries derived from the closest open field lines versus boundaries derived from the outer edge of closed field lines (see Figure 4.10). On top of this error the visualization bias is added, again without the point-and-click accuracy. This has the same reason as for Method A, where the other sources of uncertainty are dominating.

In strong agreement with Method B are also the results of the brute force matching in Method C (see Figure 4.17). While eclipse images ease the identification of loop apexes dramatically compared to coronagraph data, there is still some bias in this analysis step. While especially close to the limbs, individual field lines can be seen in form of thin plasma structures, this is not as clear higher up in the solar atmosphere. Identifying the apex of a large loop structure by visible field lines is not possible anymore and an estimation has to be made. The fact that structures are more equally illuminated over different height ranges and have sharper contours makes eclipse images still by far superior for the brute force matching implementation. This is highlighted by the agreement of the results of this analysis with the outcomes of the streamer width analysis. In fact, this same analysis using coronagraph images was done, but yielded highly variable results.

The combination of all sub-steps is leading to the final conclusion that $[R_{scs} = 2.0R_{\odot}, R_{ss} = 2.4R_{\odot}]$ is the ideal parameter set. This final parameter set is in the expected range of heights, with R_{ss} being close to the commonly used 2.5 $R_{\odot}$ (Mackay and Yeates, 2012). The configuration is valued slightly lower than EUHFORIA's default heights (cf. Section 2.2). In some cases it seems appropriate though to implement a more complex form of the model, allowing for a non-spherical source surface to adapt to different magnetic regions.

The most strict sub-step in the assessment scheme is the feature matching, where only 11 configurations passed for each date. It is clear that a certain amount of subjectivity can impact the outcomes significantly, especially in the visual inspection part. This may also influence the strictness of each sub-step. On the other hand, the way the system was applied made it possible to reduce the 67 parameter configurations down to two for only using two simulation dates. The strength is clearly located in the diversity of measures and metrics. Thus, the passing configurations appear accurate

in the field line picture, produce well matching topology when comparing to EUV and model physical properties of structures seen in white-light data fairly well.

6 Summary and Outlook

The coronal magnetic field model of the space weather simulation code EUHFORIA was investigated and a parameter study was carried out. To accomplish this, 67 different parameter sets are set-up and used in the simulation of two solar eclipse dates, being 01-Aug-2008 and 11-Jul-2010. For the quality assessment of the different configurations a benchmarking system was developed. This system builds upon a) visual quantification of the computed field lines compared to white-light data, b) magnetic topology analysis compared to EUV Carrington maps and c) semi-automatized feature matching of field line structures in the simulation data and solar eclipse images. The final result of the analysis yields that the best parameter set (i.e., the parameters that performed best on both dates that were investigated) is $[R_{scs} = 2.0R_{\odot}, R_{ss} = 2.4R_{\odot}]$. Thus, moderate values for both R_{scs} and R_{ss}, leaning towards the lower end of the parameter spectrum with a distance of 0.3 $R_{\odot}$ between the two heights are favored.

In the frame of this analysis, the developed assessment scheme proved to be of good use for judging the quality of EUHFORIA's magnetic field model. The strength of the developed benchmarking system is that it is not only applicable to EUHFORIA, but can be applied to every kind of coronal magnetic field model as long as field lines and topology can be calculated. While the rough scheme is set, there is a lot of freedom in the choice of parameters, metrics and strictness of each sub-step. This makes customization to the model or model configurations of interest possible. Moreover, it is not at all required to follow the system in the presented order of Section 4. The presented implementations can be viewed as an exemplary application of the benchmarking system.

From observational side, white-light data as well as EUV Carrington maps are required. It should be noted that while coronagraph data is fine, especially good comparisons can be achieved with the use of highly resolved solar eclipse photographs, as loop structures etc. can be viewed in great detail. Combination with STEREO satellite data makes for a great comparison dataset, as one then has three perspectives to investigate. This not only increases the sample size for the analysis, but also provides a more complete information of the global state of the corona. With the stereoscopic view it also allows for triangulation to find out exact locations of various coronal features. If one aims for using both STEREO A and B data and solar

eclipse images from Druckmüller, the possible dates to simulate reduce to 01-Aug-2008, 22-Jul-2009, 11-Jul-2010, 13-Nov-2012 and 03-Nov-2013. It is noteworthy though that compromises have to be made between unfavorable positioning of the STEREO spacecraft at earlier dates (where the lower angular separation between the two satellites gives less of a stereoscopic view) and instrumental degradation effects on the coronagraphs as well as the phase of solar activity at the given date.

While visual inspection of the model results and classification based on field line overplots onto coronagraphic image data may be quite subjective (and thus results may vary with different users), it is a viable tool when combining with more rigorous methods. This combination can also be used as some kind of pre-selection process to exclude weakly performing configurations or models from further analysis of this three-staged scheme. The best application of a pre-selection scheme is found in the combination of the visual classification and the topology analysis, as this combines two different observational sources and investigate different properties of the model output. Although we were investigating the bulk of 67 configurations for both of our target dates, no pre-selection was done to see the model's behavior throughout all simulated parameter sets.

For the topology analysis one may prefer a certain metric over the other depending on the main objective that a user has in mind for some model(s)/configuration(s). The parameters are given as examples of what may be of interest, but there are of course more possibilities for metrics and systems on how to judge the topological quality of the computed magnetic fields.

The feature matching section of the benchmarking system leaves a lot of freedom as well. More mathematical (and less empirical than the point-and-click algorithms that are used here) implementations can be thought of, depending on the purpose of the analysis. There are also more possibilities for physical/geometrical quantities of white-light structures that can be investigated in this sub-step.

While a multitude of data was used for the presented analysis in Section 4, an extension of the research with more dates is needed to arrive at a solid final conclusion regarding finding an ideal parameter set. The developed classification system shows promises in its applicability not only to the presented study on EUHFORIA, but could also be applied to other coronal magnetic field models. The standardization of assessing the quality of a solar magnetic field simulation would be the next step to enhance the comparability of model performances, where ultimately space weather modelling can greatly benefit.

Bibliography

Arge, C. Nick, Carl J. Henney, Josef Koller, et al. (Mar. 2010). „Air Force Data Assimilative Photospheric Flux Transport (ADAPT) Model“. In: *Twelfth International Solar Wind Conference*. Ed. by M. Maksimovic, K. Issautier, N. Meyer-Vernet, M. Moncuquet, and F. Pantellini. Vol. 1216. American Institute of Physics Conference Series, pp. 343–346. DOI: 10.1063/1.3395870 (cit. on p. 27).

Arge, Charles N., Dusan Odstrcil, Victor J. Pizzo, and Leslie R. Mayer (Sept. 2003). „Improved Method for Specifying Solar Wind Speed Near the Sun“. In: *Solar Wind Ten*. Ed. by Marco Velli, Roberto Bruno, Francesco Malara, and B. Bucci. Vol. 679. American Institute of Physics Conference Series, pp. 190–193. DOI: 10.1063/1.1618574 (cit. on pp. 17, 20).

Aschwanden, M. J. (2019). *New Millennium Solar Physics*. Springer-Verlag (cit. on pp. 1, 2, 4–6, 10).

Asvestari, E., S. G. Heinemann, M. Temmer, et al. (Nov. 2019). „Reconstructing Coronal Hole Areas With EUHFORIA and Adapted WSA Model: Optimizing the Model Parameters“. In: *Journal of Geophysical Research (Space Physics)* 124.11, pp. 8280–8297. DOI: 10.1029/2019JA027173. arXiv: 1907.03337 [astro-ph.SR] (cit. on pp. 13, 14, 41).

Bahcall, John N., M. H. Pinsonneault, and Sarbani Basu (July 2001). „Solar Models: Current Epoch and Time Dependences, Neutrinos, and Helioseismological Properties“. In: *The Astrophysical Journal* 555.2, pp. 990–1012. DOI: 10.1086/321493. arXiv: astro-ph/0010346 [astro-ph] (cit. on p. 2).

Bronarska, K. and G. Michalek (Jan. 2017). „Characteristics of active regions associated to large solar energetic proton events“. In: *Advances in Space Research* 59.1, pp. 384–392. DOI: 10.1016/j.asr.2016.09.011 (cit. on p. 11).

Brueckner, G. E., R. A. Howard, M. J. Koomen, et al. (Dec. 1995). „The Large Angle Spectroscopic Coronagraph (LASCO)“. In: 162.1-2, pp. 357–402. DOI: 10.1007/BF00733434 (cit. on p. 24).

Childs, Hank, Eric Brugger, Brad Whitlock, et al. (2012). „VisIt: An End-User Tool For Visualizing and Analyzing Very Large Data“. In: *High Performance Visualization–Enabling Extreme-Scale Scientific Insight*, pp. 357–372 (cit. on p. 28).

Cranmer, Steven R., Sarah E. Gibson, and Pete Riley (Nov. 2017). „Origins of the Ambient Solar Wind: Implications for Space Weather“. In: *Space Science Reviews* 212.3-4, pp. 1345–1384. DOI: 10.1007/s11214-017-0416-y. arXiv: 1708.07169 [astro-ph.SR] (cit. on pp. 6, 10, 29).

Delaboudinière, J. P., G. E. Artzner, J. Brunaud, et al. (Dec. 1995). „EIT: Extreme-Ultraviolet Imaging Telescope for the SOHO Mission“. In: 162.1-2, pp. 291–312. DOI: 10.1007/BF00733432 (cit. on p. 27).

Domingo, V., B. Fleck, and A. I. Poland (Dec. 1995). „The SOHO Mission: an Overview“. In: 162.1-2, pp. 1–37. DOI: 10.1007/BF00733425 (cit. on p. 24).

Druckmüller, M. (Dec. 2009). „Phase Correlation Method for the Alignment of Total Solar Eclipse Images“. In: *The Astrophysical Journal* 706.2, pp. 1605–1608. DOI: 10.1088/0004-637X/706/2/1605 (cit. on p. 24).

Eastwood, J. P., M. A. Hapgood, E. Biffis, et al. (Dec. 2018). „Quantifying the Economic Value of Space Weather Forecasting for Power Grids: An Exploratory Study“. In: *Space Weather* 16.12, pp. 2052–2067. DOI: 10.1029/2018SW002003 (cit. on p. 10).

Fränz, M. and D. Harper (Feb. 2002). „Heliospheric coordinate systems“. In: *Planetary and Space Science* 50.2, pp. 217–233. DOI: 10.1016/S0032-0633(01)00119-2 (cit. on p. 21).

Griffiths, D. J. (2017). *Introduction to Electrodynamics*. Cambridge University Press (cit. on pp. 6, 18).

Gudiksen, B. V., M. Carlsson, V. H. Hansteen, et al. (July 2011). „The stellar atmosphere simulation code Bifrost. Code description and validation“. In: *Astronomy and Astrophysics* 531, A154, A154. DOI: 10.1051/0004-6361/201116520. arXiv: 1105.6306 [astro-ph.SR] (cit. on p. 18).

Hale, George E., Ferdinand Ellerman, S. B. Nicholson, and A. H. Joy (Apr. 1919). „The Magnetic Polarity of Sun-Spots“. In: *The Astrophysical Journal* 49, p. 153. DOI: 10.1086/142452 (cit. on p. 8).

Hale, George E. and Seth B. Nicholson (Nov. 1925). „The Law of Sun-Spot Polarity“. In: *The Astrophysical Journal* 62, p. 270. DOI: 10.1086/142933 (cit. on p. 8).

Hanslmeier, A. (2014). *Einführung in Astronomie und Astrophysik*. Springer-Verlag (cit. on pp. 1, 3).

Harvey, J. W., F. Hill, R. P. Hubbard, et al. (May 1996). „The Global Oscillation Network Group (GONG) Project“. In: *Science* 272.5266, pp. 1284–1286. DOI: 10.1126/science.272.5266.1284 (cit. on p. 27).

Hathaway, David H. (Sept. 2015). „The Solar Cycle“. In: *Living Reviews in Solar Physics* 12.1, 4, p. 4. DOI: 10.1007/lrsp-2015-4. arXiv: 1502.07020 [astro-ph.SR] (cit. on pp. 3, 7, 9, 10, 36).

Hess Webber, S. A., N. Karna, W. D. Pesnell, and M. S. Kirk (Nov. 2014). „Areas of Polar Coronal Holes from 1996 Through 2010“. In: 289.11, pp. 4047–4067. DOI: 10.1007/s11207-014-0564-0 (cit. on pp. 28, 41).

Howard, R. A., J. D. Moses, A. Vourlidas, et al. (Apr. 2008). „Sun Earth Connection Coronal and Heliospheric Investigation (SECCHI)“. In: 136.1-4, pp. 67–115. DOI: 10.1007/s11214-008-9341-4 (cit. on p. 24).

Kaiser, M. L., T. A. Kucera, J. M. Davila, et al. (Apr. 2008). „The STEREO Mission: An Introduction“. In: 136.1-4, pp. 5–16. DOI: 10.1007/s11214-007-9277-0 (cit. on p. 24).

Karna, N., S. A. Hess Webber, and W. D. Pesnell (Sept. 2014). „Using Polar Coronal Hole Area Measurements to Determine the Solar Polar Magnetic Field Reversal in Solar Cycle 24“. In: 289.9, pp. 3381–3390. DOI: 10.1007/s11207-014-0541-7 (cit. on pp. 28, 41).

Kruse, M., V. Heidrich-Meisner, R. F. Wimmer-Schweingruber, and M. Hauptmann (June 2020). „An elliptic expansion of the potential field source surface model“. In: *Astronomy and Astrophysics* 638, A109, A109. DOI: 10.1051/0004-6361/202037734. arXiv: 2005.12843 [astro-ph.SR] (cit. on p. 57).

Lemen, James R., Alan M. Title, David J. Akin, et al. (Jan. 2012). „The Atmospheric Imaging Assembly (AIA) on the Solar Dynamics Observatory (SDO)“. In: 275.1-2, pp. 17–40. DOI: 10.1007/s11207-011-9776-8 (cit. on p. 27).

Linker, J. A., S. G. Heinemann, M. Temmer, et al. (Mar. 2021). „Coronal Hole Detection and Open Magnetic Flux“. In: *arXiv e-prints*, arXiv:2103.05837, arXiv:2103.05837. arXiv: 2103.05837 [astro-ph.SR] (cit. on p. 41).

Lionello, Roberto, Jon A. Linker, and Zoran Mikić (Jan. 2009). „Multispectral Emission of the Sun During the First Whole Sun Month: Magnetohydrodynamic Simulations“. In: *The Astrophysical Journal* 690.1, pp. 902–912. DOI: 10.1088/0004-637X/690/1/902 (cit. on p. 18).

Mackay, Duncan H. and Anthony R. Yeates (Nov. 2012). „The Sun's Global Photospheric and Coronal Magnetic Fields: Observations and Models“. In: *Living Reviews in Solar Physics* 9.1, 6, p. 6. DOI: 10.12942/lrsp-2012-6. arXiv: 1211.6545 [astro-ph.SR] (cit. on pp. 8, 13–19, 27, 60).

Mohr, Peter J., David B. Newell, and Barry N. Taylor (Sept. 2016). „CODATA recommended values of the fundamental physical constants: 2014*“. In: *Reviews of Modern Physics* 88.3, 035009, p. 035009. DOI: 10.1103/RevModPhys.88.035009. arXiv: 1507.07956 [physics.atom-ph] (cit. on p. 21).

Morgan, Huw, Shadia Rifai Habbal, and Richard Woo (July 2006). „The Depiction of Coronal Structure in White-Light Images“. In: *Solar Physics* 236.2, pp. 263–272. DOI: 10.1007/s11207-006-0113-6. arXiv: astro-ph/0602174 [astro-ph] (cit. on p. 25).

Pesnell, W. Dean, B. J. Thompson, and P. C. Chamberlin (Jan. 2012). „The Solar Dynamics Observatory (SDO)“. In: 275.1-2, pp. 3–15. DOI: 10.1007/s11207-011-9841-3 (cit. on p. 27).

Pomoell, Jens and S. Poedts (June 2018). „EUHFORIA: European heliospheric forecasting information asset“. In: *Journal of Space Weather and Space Climate* 8, A35, A35. DOI: 10.1051/swsc/2018020 (cit. on pp. i, iii, 17, 19–22).

Riley, Pete, J. A. Linker, Z. Mikić, et al. (Dec. 2006). „A Comparison between Global Solar Magnetohydrodynamic and Potential Field Source Surface Model Results“. In: *The Astrophysical Journal* 653.2, pp. 1510–1516. DOI: 10.1086/508565 (cit. on pp. 13, 15, 16).

Rodríguez Gómez, Jenny Marcela, Judith Palacios, Luis E. A. Vieira, and Alisson Dal Lago (Oct. 2019). „The Plasma β Evolution through the Solar Corona during Solar Cycles 23 and 24“. In: *The Astrophysical Journal* 884.1, 88, p. 88. DOI: 10.3847/1538-4357/ab40af. arXiv: 1910.00894 [astro-ph.SR] (cit. on p. 7).

Schatten, K. H. (Jan. 1971). „Current sheet magnetic model for the solar corona.“ In: *Cosmic Electrodynamics* 2, pp. 232–245 (cit. on p. 15).

Schwenn, Rainer (Aug. 2006). „Space Weather: The Solar Perspective“. In: *Living Reviews in Solar Physics* 3.1, 2, p. 2. DOI: 10.12942/lrsp-2006-2 (cit. on pp. 10, 11).

Seaton, D. B., D. Berghmans, B. Nicula, et al. (Aug. 2013). „The SWAP EUV Imaging Telescope Part I: Instrument Overview and Pre-Flight Testing“. In: 286.1, pp. 43–65. DOI: 10.1007/s11207-012-0114-6. arXiv: 1208.4631 [astro-ph.IM] (cit. on p. 28).

Temmer, Manuela (Apr. 2021). „Space weather: the solar perspective – an update to Schwenn (2006)“. In: *arXiv e-prints*, arXiv:2104.04261, arXiv:2104.04261. arXiv: 2104.04261 [astro-ph.SR] (cit. on p. 11).

Temmer, Manuela, Tanja Rollett, Christian Möstl, et al. (Dec. 2011). „Influence of the Ambient Solar Wind Flow on the Propagation Behavior of Interplanetary Coronal Mass Ejections“. In: *The Astrophysical Journal* 743.2, 101, p. 101. DOI: 10.1088/0004-637X/743/2/101. arXiv: 1110.0827 [astro-ph.SR] (cit. on p. 11).

Vourlidas, Angelos and Russell A. Howard (May 2006). „The Proper Treatment of Coronal Mass Ejection Brightness: A New Methodology and Implications for Observations“. In: *The Astrophysical Journal* 642.2, pp. 1216–1221. DOI: 10.1086/501122 (cit. on p. 5).

Wang, Y. M. and Jr. Sheeley N. R. (June 1990). „Solar Wind Speed and Coronal Flux-Tube Expansion“. In: *The Astrophysical Journal* 355, p. 726. DOI: 10.1086/168805 (cit. on p. 17).

Zhao, Xuepu and J. Todd Hoeksema (Apr. 1994). „A Coronal Magnetic Field Model with Horizontal Volume and Sheet Currents“. In: 151.1, pp. 91–105. DOI: 10.1007/BF00654084 (cit. on p. 16).

A

EUHFORIA Parameter Configurations

Table A.1.: Used parameter sets for the analysis carried out in Chapter 4.

Configuration Number	$R_{\mathrm{scs}}[\mathrm{R}_{\odot}]$	$R_{\mathrm{ss}}[\mathrm{R}_{\odot}]$
1	1.3	1.4
2	1.3	1.7
3	1.3	2.0
4	1.3	2.3
5	1.3	2.6
6	1.3	2.9
7	1.3	3.2
8	1.4	1.5
9	1.4	1.8
10	1.4	2.1
11	1.4	2.4
12	1.4	2.7
13	1.4	3.0
14	1.5	1.6
15	1.5	1.9
16	1.5	2.2
17	1.5	2.5
18	1.5	2.8
19	1.5	3.1
20	1.6	1.7
21	1.6	2.0
22	1.6	2.3
23	1.6	2.6
24	1.6	2.9
25	1.6	3.2
26	1.7	1.8
27	1.7	2.1
28	1.7	2.4
29	1.7	2.7
30	1.7	3.0

31	1.8	1.9
32	1.8	2.2
33	1.8	2.5
34	1.8	2.8
35	1.8	3.1
36	1.9	2.0
37	1.9	2.3
38	1.9	2.6
39	1.9	2.9
40	1.9	3.2
41	2.0	2.1
42	2.0	2.4
43	2.0	2.7
44	2.0	3.0
45	2.1	2.2
46	2.1	2.5
47	2.1	2.8
48	2.1	3.1
49	2.2	2.3
50	2.2	2.6
51	2.2	2.9
52	2.2	3.2
53	2.3	2.4
54	2.3	2.7
55	2.3	3.0
56	2.4	2.5
57	2.4	2.8
58	2.4	3.1
59	2.5	2.6
60	2.5	2.9
61	2.5	3.2
62	2.6	2.7
63	2.6	3.0
64	2.7	2.8
65	2.7	3.1
66	2.8	2.9
67	2.8	3.2

Colophon

This thesis was typeset with LaTeX 2$_\varepsilon$. It uses the *Clean Thesis* style developed by Ricardo Langner, available at http://cleanthesis.der-ric.de/. The design of the *Clean Thesis* style is inspired by user guide documents from Apple Inc.

The template was adapted by Desmond Grossmann, BSc, Stefan Janisch, BSc, Lea Schimak and Paul Beck, PhD to implement the editorial guidelines of *Astronomy & Astrophysics* and the cooperate-identity guidelines of the University of Graz for the Institute for Physics. This thesis uses the template, released on the webpage of the *Department for Geophysics, Astrophysics and Meteorology (IGAM)*[1] on *February 12, 2021*.

[1] https://physik.uni-graz.at/de/igam/